MOX–Report No. 27/2013

Isogeometric Analysis and Error Estimates for High Order Partial Differential Equations in Fluid Dynamics

Tagliabue, A.; Dedè, L.; Quarteroni, A.

Isogeometric Analysis and Error Estimates for High Order Partial Differential Equations in Fluid Dynamics

Anna Tagliabue [1,*], Luca Dedè [2], and Alfio Quarteroni [1,2]

[1] MOX – Modeling and Scientific Computing,
Mathematics Department "F. Brioschi",
Politecnico di Milano,
via Bonardi 9, Milano, 20133, Italy.

[2] CMCS – Chair of Modeling and Scientific Computing,
MATHICSE – Mathematics Institute of Computational Science and Engineering,
EPFL – École Polytechnique Fédérale de Lausanne,
Station 8, Lausanne, CH – 1015, Switzerland.

Abstract

In this paper, we consider the numerical approximation of high order Partial Differential Equations (PDEs) by means of NURBS–based Isogeometric Analysis (IGA) in the framework of the Galerkin method, for which global smooth basis functions with degree of continuity higher than $\mathcal{C}^0$ can be used. We derive a priori error estimates for high order elliptic PDEs under h–refinement, by extending existing results for second order PDEs approximated with IGA and specifically addressing the case of errors in lower order norms. We present some numerical results which both validate the proposed error estimates and highlight the accuracy of IGA. Then, we apply NURBS–based IGA to solve the fourth order stream function formulation of the Navier–Stokes equations; in particular, we solve the benchmark lid–driven cavity problem for Reynolds numbers up to 5,000.

Key words. High order Partial Differential Equations; Isogeometric Analysis; a priori error estimates; Navier–Stokes equations; stream function formulation.

1 Introduction

The numerical approximation of high order Partial Differential Equations (PDEs) represents a challenging task for the classical Galerkin Finite Element Methods due to the need to use trial and test functions featuring high degree of continuity. This issue has been addressed by adapting existing finite element schemes or developing new numerical schemes. Specifically, the Discontinuous Galerkin (DG) [40] and local discontinuous Galerkin (LDG) methods, firstly introduced in [15], were developed and adapted for solving high order PDEs; see e.g. [34] for fourth order PDEs and the references therein for more general cases. Analogously, non–conforming discretizations have been used to achieve the needed global regularity [13]; additionally, ad hoc techniques as continuous/discontinuous finite element approximations for fourth order

---

[*] Corresponding author. E–mail: anna.tagliabue@polimi.it, Phone: +39 02 2399 4604, Fax: +39 02 2399 4586.

PDEs have been developed in [21] in order to overcome the issue of defining $\mathcal{C}^1$-continuous basis for arbitrary shaped elements in dimensions greater than one. Currently, the golden standard in the framework of the standard Galerkin method with Lagrangian basis functions, consists in resorting to mixed formulations [24]. Spectral or pseudo-spectral domain decomposition techniques have also been used to approximate fourth order PDEs resulting from the Navier–Stokes equations in stream function formulation, see [36].

Isogeometric Analysis (IGA) is a recently developed computational methodology initiated with the work of Hughes et al. in [16] aiming at closing the existing gap between Computed Aided Design (CAD) and Finite Element Analysis (FEA). Based on the isogeometric paradigm, for which the same basis functions used to represent the known geometry are then used to approximate the unknown solution of the PDEs, IGA has been successfully used for the numerical approximation of a wide range of problems providing accurate and efficient solutions. An extensive discussion on the solution of both linear and nonlinear equations governing elasticity or fluid dynamics problems by means of IGA is provided in [17]. Moreover, IGA provides advantages in the numerical approximation of high order PDEs within the framework of the standard Galerkin formulation, since in IGA globally smooth basis functions can be eventually used. In particular, we refer to NURBS–based IGA, due to the large use of NURBS (Non–Uniform Rational B-Splines) [37] within the CAD technology, and above all, for the mathematical properties of these basis functions. We observe that, besides the possibility of offering simplified refinements procedures, NURBS allow to exactly represent some common geometries in engineering design, e.g. conic sections.

One of the major features of NURBS, which allows efficient numerical approximations of high order PDEs in the framework of the Galerkin method, consists in the fact that NURBS basis functions can be globally $\mathcal{C}^k$–continuous in the computational domain, with $k \geq 0$. This property allows a direct discretization of the weak form of the problem without the need to resort to mixed formulations, as typically is the case of FEA. In this respect, NURBS–based IGA has already been successfully used to solve high order PDEs. In [27, 32] the fourth–order Cahn–Hillard equations have been solved, while in [9, 19, 28] high order phase field models have been used for fracture modeling, topology optimization, and crystal growth, respectively. In [7, 8] structural problems for shell and plates have been solved with IGA, specifically Kirchhoff-Love models. In [2] a stream function, high order formulation has been used to solve planar elastic problems within the IGA framework, for which an estimation of the convergence rates of the errors with respect to the mesh size has been performed numerically. However, despite a significant numerical evidence, a complete, theoretical error analysis for high order PDEs has not been performed yet, especially for errors in lower order norms.

In this work, we provide a priori error estimates under h–refinement for the NURBS–based IGA approximation of high order scalar elliptic PDEs, extending the results presented in [3] for second order PDEs. Specifically, we review some approximation results presented in [3] and we focus on the derivation of the errors in lower order norms by means of Aubin–Nietsche's arguments [35, 43]. We highlight the dependence of the convergence rates on the order of the spatial differential operators, the regularity of the solutions, and the degree of the basis functions used. The convergence rates of the approximation errors of the IGA–Galerkin method with respect to the global mesh size h are verified by means of numerical tests with fourth and sixth order scalar PDEs.

As application, we consider the numerical approximation of the Navier–Stokes equations in stream function formulation [39], for which the incompressibility condition is fulfilled exactly in the computational domain; in this case, the standard Galerkin formulation yields a stable problem by construction. Specifically, we present a numerical study by means of NURBS–based IGA for the benchmark lid–driven cavity problem by comparing the results, up to Reynolds number 5,000, with those available in literature. Namely, we refer to [10], which considers a spectral Chebychev collocation method, [22], where divergence–conforming B–Splines discretizations in the framework of IGA are developed, and [25], where a multigrid technique applied to finite difference approximations of the vorticity–stream function formulation of the Navier–Stokes equations is used.

The outline of this work is as follows. In Section 2, we recall the basic notions of NURBS–based IGA in the framework of the Galerkin method, specifically for high order scalar elliptic PDEs. In Section 3, we derive the a priori error estimates. In Section 4, we present, in view of the numerical tests, some high order PDEs and discuss the numerical approximation schemes. Finally, in Section 5, we report and discuss the numerical results. Conclusions follow.

2 NURBS–based Isogeometric Analysis

In this section, we recall the basic concepts of the B–Splines and NURBS basis functions and geometrical representation. Then, in Section 2.2, we briefly describe NURBS–based IGA in the framework of the Galerkin method for the solution of high order PDEs. For an extensive overview of B–Splines and NURBS, see for instance [17, 37]; for more details related to NURBS–based IGA, we refer the interested reader to e.g. [16, 17, 18]. The notation used in this work is similar to the one used in [3, 6].

2.1 B–Splines and NURBS

A *knot vector* is a set of non–decreasing real numbers, representing coordinates in the *parameter space*. We indicate the knot vector as $\Xi = \{\xi_1, \xi_2, \ldots, \xi_{n+p+1}\}$, where ξ_i is the i–th knot, with the knot index $i \in \{1, \ldots, n+p+1\}$ characterized by the polynomial degree p and the number of basis functions n defining the B–Splines basis, respectively. By convention, we assume that $\xi_1 = 0$ and $\xi_{n+p+1} = 1$, such that the parametric domain is defined as $\widehat{\Omega} := (\xi_1, \xi_{n+p+1}) = (0,1) \subset \mathbb{R}$. Knots may be repeated with the number of repetitions indicating its *multiplicity*. A knot vector is said to be *open* if its first and last knots appear $p+1$ times; specifically, in this work we consider this case. In order to introduce the concept of *mesh* elements in the parametric domain, we collect all the r distinct and ordered knots of Ξ, say ζ_j for $j = 1, \ldots, r$, into a vector $\mathcal{Z} = \{\zeta_1, \ldots, \zeta_r\}$, with $\zeta_1 \equiv \xi_1 = 0$ and $\zeta_r \equiv \xi_{n+p+1} = 1$. In particular, the one dimensional *mesh* over $\widehat{\Omega}$, say $\mathcal{Q}_h$, is defined as the collection of the subdomains bounded by two distinct knots, i.e.:

$$\mathcal{Q}_h := \{Q = (\zeta_j, \zeta_{j+1}) \, : \, j = 1, \ldots, r-1\}; \tag{2.1}$$

we indicate with $\widehat{h} := \max\{\widehat{h}_Q \, : \, Q \in \mathcal{Q}_h\}$ the *global mesh size* in the parametric domain $\widehat{\Omega}$, where $\widehat{h}_Q := \mathrm{diam}(Q)$ for all $Q \in \mathcal{Q}_h$. Moreover, since the multiplicity of the knots has important implications in the regularity properties of the basis functions, an auxiliary vector is defined in relation with $\mathcal{Z}$; specifically, we introduce the vector $\mathcal{M} := \{m_1, \ldots, m_r\}$, with $m_j \geq 1$ representing the multiplicity of the knot value ζ_j, for $j = 1, \ldots, r$.

By means of the *Cox–de Boor recursion formula* [17, 37], univariate B–Splines basis functions $N_i : \widehat{\Omega} \rightarrow \mathbb{R}$ for $i = 1, \ldots, n$, are built as piecewise polynomials of degree p with compact support over the interval (ξ_i, ξ_{i+p+1}). The basis functions are everywhere pointwise nonnegative and $\mathcal{C}^\infty$–continuous, except in the knot values ζ_j, where they are only $\mathcal{C}^{p-m_j}$–continuous. In particular, we define for all $j = 1, \ldots, r$, the smoothness integer parameters $k_j = p - m_j + 1$ such that $0 \leq k_j \leq p$, we collect them in a vector $\mathcal{K} = \{k_1, \ldots, k_r\}$, and we introduce the minimum integer parameter $k_{\min} := \min\limits_{j=2,\ldots,r-1} \{k_j\}$. We observe that, according to the definition of the vector $\mathcal{K}$, in the knot ζ_j, for $j = 1, \ldots, r$, the basis functions are $\mathcal{C}^{k_j-1}$–continuous. The B–Splines space built from the basis functions in the parametric domain $\widehat{\Omega}$ reads:

$$\mathcal{S}_h := \mathrm{span}\, \{N_i\}_{i=1}^n \, . \tag{2.2}$$

By definition, the B-Splines in $\mathcal{S}_h$ are globally $\mathcal{C}^{k_{\min}}$–continuous. An example of B–Splines basis functions of degree $p = 2$, exhibiting different regularities across the knots, is provided in Figure 1.

The tensor product structure allows to extend the definition of the B–Splines space to the κ–dimensional case. Starting from κ knot vectors $\Xi_\alpha = \{\xi_1^\alpha, \xi_2^\alpha, \ldots, \xi_{n_\alpha+p_\alpha+1}^\alpha\}$ for $\alpha = 1, \ldots, \kappa$, we provide the corresponding vectors $\mathcal{Z}_\alpha = \{\zeta_1^\alpha, \ldots, \zeta_{r_\alpha}^\alpha\}$ and $\mathcal{M}_\alpha = \{m_1^\alpha, \ldots, m_{r_\alpha}^\alpha\}$. A *mesh* $\mathcal{Q}_h$ in the parametric domain $\widehat{\Omega} = (0,1)^\kappa$ is defined by its partition into κ–dimensional elements, as:

$$\mathcal{Q}_h := \left\{ Q := \otimes_{\alpha=1}^\kappa (\zeta_{j_\alpha}^\alpha, \zeta_{j_\alpha+1}^\alpha), \; 1 \leq j_\alpha \leq r_\alpha - 1 \right\}. \tag{2.3}$$

Moreover, as for the univariate case, having set the element size $\widehat{h}_Q := \mathrm{diam}(Q)$ for all $Q \in \mathcal{Q}_h$, the global mesh size reads $\widehat{h} := \max\limits_{Q \in \mathcal{Q}_h} \{\widehat{h}_Q\}$. For each multi–index $\boldsymbol{i} := (i_1, \ldots, i_\kappa)$ in the set $I = \{\boldsymbol{i} = (i_1, \ldots, i_\kappa) : 0 \leq i_\alpha \leq n_\alpha, \text{ for } 1 \leq \alpha \leq \kappa\}$, we define the *multivariate* B–Splines basis functions as:

$$N_{\boldsymbol{i}} \, : \, \widehat{\Omega} \rightarrow \mathbb{R}, \qquad N_{\boldsymbol{i}}(\boldsymbol{\eta}) := \prod_{\alpha=1}^{\kappa} N_{i_\alpha}^\alpha(\eta_\alpha), \tag{2.4}$$

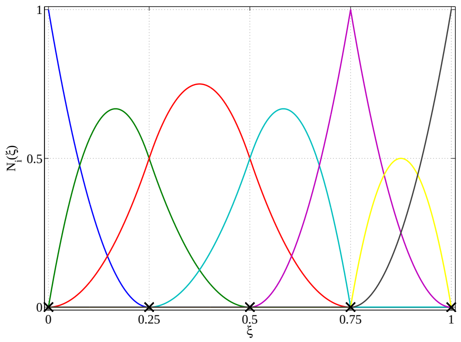

Figure 1: B–Splines basis functions of degree $p = 2$ obtained from the open knot vector $\Xi = \{0, 0, 0, 1/4, 1/2, 3/4, 3/4, 1, 1, 1\}$ with $n = 7$, $\mathcal{Z} = \{0, 1/4, 1/2, 3/4, 1\}$, $\mathcal{M} = \{3, 1, 1, 2, 3\}$, and $\mathcal{K} = \{0, 2, 2, 1, 0\}$. The basis functions are only $\mathcal{C}^0$–continuous in the knot value $\zeta_4 = 3/4$, while $\mathcal{C}^1$–continuous in the knot values $\zeta_2 = 1/4$ and $\zeta_3 = 1/2$.

and we denote the tensor product B–Splines space, as:

$$\mathcal{S}_h := \text{span}\,\{N_{\boldsymbol{i}}\}_{\boldsymbol{i} \in I}\,. \tag{2.5}$$

The (directional) regularity of each basis function $N_{\boldsymbol{i}}$ can be deduced by the regularity of the univariate functions defining $N_{\boldsymbol{i}}$ in virtue of the tensor product structure. In particular, in parallel with the one dimensional case, we can refer to smoothness integer parameters and define for each parametric direction $\alpha = 1, \ldots, \kappa$ the vectors $\mathcal{K}^\alpha = \{k_1^\alpha, \ldots, k_{r_\alpha}^\alpha\}$ and the minimum integer parameters as $k_{\min}^\alpha := \min\limits_{j_\alpha = 2, \ldots, r_\alpha - 1} \{k_{j_\alpha}^\alpha\}$. The basis functions are $\mathcal{C}^\infty$–continuous in the interior of each element $Q \in \mathcal{Q}_h$, while, across each internal non-zero dimensional face separating the elements, the regularity can be still defined by referring to the (directional) regularity in each parametric α–direction. Specifically, by considering an integer $l \leq \kappa$ and a set $\mathcal{B} \subseteq \{1, \ldots, \kappa\}$ such that $|\mathcal{B}| = l$, a $(\kappa - l)$–dimensional face is identified by l fixed knots $\zeta_{j_\beta}^\beta$ for each β–parametric direction such that $\beta \in \mathcal{B}$ and with $1 \leq j_\beta \leq r_\beta - 1$. Across such face, a basis function is $\mathcal{C}^{\overline{k}-1}$–continuous, with $\overline{k} := \min\limits_{\beta \in \mathcal{B}} k_{j_\beta}^\beta$, i.e. the regularity is equal to the minimum over each parametric α–direction of the maximum regularity across this face for each parametric direction. Moreover, by defining the regularity constant $k_{\min} := \min\limits_{\alpha = 1, \ldots, \kappa} \{k_{\min}^\alpha\}$, it is straightforward to deduce that the B-Splines basis functions of $\mathcal{S}_h$ are at least globally $\mathcal{C}^{k_{\min}}$–continuous.

Uni– and multivariate NURBS basis functions are defined on the parametric domain $\widehat{\Omega} = (0, 1)^\kappa$ once provided κ knot vectors Ξ_α for $\alpha = 1, \ldots, \kappa$ and the corresponding B–Splines basis $\{N_{\boldsymbol{i}}\}_{\boldsymbol{i} \in I}$, by introducing a set of real numbers $\boldsymbol{\omega} = \{\omega_{\boldsymbol{i}}\}_{\boldsymbol{i} \in I}$, called the *weights*. We assume that the weights are positive and we define a positive scalar piecewise polynomial function, called *weighting function*, as:

$$W : \widehat{\Omega} \to \mathbb{R}, \qquad W(\boldsymbol{\eta}) := \sum_{\boldsymbol{i} \in I} \omega_{\boldsymbol{i}} N_{\boldsymbol{i}}(\boldsymbol{\eta}). \tag{2.6}$$

The $\boldsymbol{i}$-th multivariate NURBS basis function is defined as:

$$R_{\boldsymbol{i}} : \widehat{\Omega} \to \mathbb{R}, \qquad R_{\boldsymbol{i}}(\boldsymbol{\eta}) = \frac{N_{\boldsymbol{i}}(\boldsymbol{\eta}) \omega_{\boldsymbol{i}}}{W(\boldsymbol{\eta})} \qquad \forall \boldsymbol{i} \in I, \tag{2.7}$$

and the corresponding NURBS space over the parametric domain $\widehat{\Omega}$ reads:

$$\mathcal{N}_h := \text{span}\,\{R_{\boldsymbol{i}}\}_{\boldsymbol{i} \in I}\,. \tag{2.8}$$

In the framework of NURBS–based IGA the computational domain Ω, in which the PDEs are defined, is represented by a NURBS entity; specifically, we consider the case of geometries that can be modeled as a single *patch*. NURBS geometrical entities of dimension $\kappa \geq 1$ are defined in the physical space $\mathbb{R}^d$ with

$1 \leq \kappa \leq d$; for more details see e.g. [20]. In particular, by considering the NURBS space over the parametric domain $\widehat{\Omega}$ of Eq. (2.8) and a set of *control points* $\{\boldsymbol{P_i}\}_{\boldsymbol{i}\in I} \subseteq \mathbb{R}^d$, a NURBS geometry Ω in $\mathbb{R}^d$ is defined from the parametric domain $\widehat{\Omega} = (0,1)^\kappa$ by means of the *geometrical mapping*:

$$\mathbf{x} : \widehat{\Omega} \to \Omega \subseteq \mathbb{R}^d, \qquad \mathbf{x}(\boldsymbol{\eta}) = \sum_{\boldsymbol{i}\in I} R_{\boldsymbol{i}}(\boldsymbol{\eta})\boldsymbol{P_i}. \tag{2.9}$$

In virtue of the geometrical mapping (2.9), we define the *physical mesh* in the physical domain Ω, whose elements are obtained from Eq. (2.9) as the image of the elements in the parametric domain, i.e.:

$$\mathcal{K}_h := \{K = \mathbf{x}(Q) \ : \ Q \in \mathcal{Q}_h\}. \tag{2.10}$$

Moreover, we define the space of NURBS in the domain Ω as the push–forward of the space $\mathcal{N}_h$ of Eq. (2.8), i.e.:

$$\mathcal{V}^h := \operatorname{span}\left\{R_{\boldsymbol{i}} \circ \mathbf{x}^{-1}\right\}_{\boldsymbol{i}\in I} = \operatorname{span}\left\{\mathcal{R}_{\boldsymbol{i}}\right\}_{\boldsymbol{i}\in I}, \tag{2.11}$$

where $\{\mathcal{R}_{\boldsymbol{i}}\}_{\boldsymbol{i}\in I}$ is the NURBS basis in the physical domain, with $\mathcal{R}_{\boldsymbol{i}} := R_{\boldsymbol{i}} \circ \mathbf{x}^{-1}$ for all $\boldsymbol{i} \in I$. The geometrical mapping (2.9) is assumed to be invertible a.e. in Ω, with smooth inverse on each element K of the physical mesh $\mathcal{K}_h$.

In our analysis we restrict to the case in which the dimension d of the physical space $\mathbb{R}^d$ is equal to the dimension κ of the parameter space $\mathbb{R}^\kappa$, i.e. $d = \kappa$. The case $\kappa < d$ is addressed e.g. in [20].

2.2 NURBS-based Isogeometric Analysis: the Galerkin method

We recall NURBS–based IGA in the framework of the Galerkin method for the approximation of PDEs by considering the case of high order scalar elliptic PDEs.

Let us consider a domain $\Omega \subset \mathbb{R}^d$ described by NURBS and a well–posed scalar elliptic PDE of order $2m$, with $m \geq 1$, whose variational formulation reads:

$$\text{find } u \in V \quad : \quad a(u,v) = F(v) \quad \forall v \in V, \tag{2.12}$$

where $V \subseteq H^m(\Omega)$ is a Hilbert space endowed with the norm of V and whose functions satisfy the homogeneous counterpart of the essential boundary conditions; specifically, $H^m(\Omega) := \Big\{ v \in L^2(\Omega) \ : \ D^{(\boldsymbol{\iota})} v \in L^2(\Omega)$ for all $\boldsymbol{\iota} = (\iota_1, \ldots, \iota_d) \in \mathbb{N}^d$ with $0 \leq |\boldsymbol{\iota}| = \iota_1 + \ldots + \iota_d \leq m \Big\}$, where $D^{(\boldsymbol{\iota})}$ is the distributional partial derivative, see e.g. [1]. Moreover, $a : V \times V \to \mathbb{R}$ is a continuous, (strongly) coercive, and bilinear form with continuity and coercivity constants M and α_c, respectively; $F : V \to \mathbb{R}$ is a linear and continuous functional. In this manner the hypotheses of the *Lax–Milgram Lemma* (see for instance [35, 40]) hold, ensuring the existence and uniqueness of the solution of problem (2.12).

When considering NURBS–based IGA, we look for an approximate solution of problem (2.12) which is an element of the NURBS space $\mathcal{V}^h$ of Eq. (2.11). In particular, the real valued approximate solution of problem (2.12) is expressed as:

$$u_h : \Omega \to \mathbb{R}, \qquad u_h(\mathbf{x}) = \sum_{\boldsymbol{i}\in I} \mathcal{R}_{\boldsymbol{i}}(\mathbf{x}) d_{\boldsymbol{i}} = \sum_{\boldsymbol{i}\in I} R_{\boldsymbol{i}}(\mathbf{x}^{-1}(\mathbf{x})) d_{\boldsymbol{i}}, \tag{2.13}$$

where $\{\mathcal{R}_{\boldsymbol{i}}\}_{\boldsymbol{i}\in I}$ is the NURBS basis in the physical domain Ω, while $\{d_{\boldsymbol{i}}\}_{\boldsymbol{i}\in I} \subseteq \mathbb{R}$ are the *control variables.*

Remark 2.1. *The subscript h in Eq.* (2.13) *refers to the characteristic size of the mesh elements, introduced in Section 2.1 and highlights the definition of functions over the finite dimensional NURBS space $\mathcal{V}^h$ of Eq.* (2.11)*. Usually, the computational domain Ω is represented at the coarsest level of discretization and refinement procedures are performed according to accuracy requirements aiming at improving the approximation of the solution by enriching the NURBS space $\mathcal{V}^h$. With NURBS basis functions, three kinds of refinement can be performed, namely h–, p–, k–refinements; we refer the reader to [16, 17] for a detailed description. We recall that these refinements allow to control the element size, the degree, and the regularity of the basis functions in a flexible manner. Moreover, we remark that the refinement procedures are performed in such a way that the geometrical mapping* (2.9) *is preserved at the coarsest level of discretization.*

In the framework of the finite-dimensional Galerkin method, the approximate solution u_h of problem (2.12) is obtained by solving the following problem:

$$\text{find } u_h \in V^h \quad : \quad a(u_h, v_h) = F(v_h) \quad \forall v_h \in V^h, \tag{2.14}$$

with $V^h \subseteq V$ a nontrivial and finite dimensional subspace, specifically defined as $V^h := V \cap \mathcal{V}^h$, where $\mathcal{V}^h$ is the NURBS space introduced in Eq. (2.11). The well–posedness of problem (2.14) is determined in the following approximation theorem (see for instance [35, 40]).

Theorem 2.1. *Let the hypotheses of Lax–Milgram Lemma be satisfied, i.e.* $a(\cdot,\cdot)$ *and* $F(\cdot)$ *are a continuous, strongly coercive and bilinear form and a linear and continuous functional, respectively (see Eq.* (2.12)*). Then, there exists a unique solution* $u_h \in V_h$ *of problem* (2.14) *and the following stability estimate holds:*

$$\|u_h\|_V \leq \frac{1}{\alpha_c} \|F\|_{V'}. \tag{2.15}$$

Moreover, the approximation error $e_h := u - u_h$*, with* u *the unique solution of problem* (2.12)*, satisfies the optimal error estimate:*

$$\|u - u_h\|_V \leq \frac{M}{\alpha_c} \inf_{v_h \in V^h} \|u - v_h\|_V. \tag{2.16}$$

Remark 2.2. *When considering (high order) PDEs of order* $2m$*, with* $m > 1$*, the weak form of problem* (2.12) *exhibits derivatives of the solution and test functions up to the order* m*. The numerical approximation of problem* (2.12) *by means of the Galerkin method* (2.14) *requires that the basis functions are at least globally* $\mathcal{C}^{m-1}$*–continuous in* Ω*. However, in the standard FEA setting, the Lagrangian basis functions are only globally* $\mathcal{C}^0$*–continuous, for which it is necessary e.g. to increase the number of variables, as it is the case of mixed formulations. Conversely, NURBS–based IGA, for which we can build basis functions with the required regularity up to the* $\mathcal{C}^{m-1}$*–continuity, allows the use of the standard Galerkin formulation in a straightforward and efficient manner.*

3 A priori error estimates for high order PDEs

In this section we provide the *a priori error estimates* for the errors associated to the NURBS–based IGA approximation of linear scalar elliptic PDEs of order $2m$. The result generalizes the a priori error estimate provided in [3] for second order elliptic operators and it is based on the use of the *Aubin–Nietsche's argument* for the derivation of the error in lower order norms; see for instance [35, 43]. For simplicity, we consider the case of high order ($2m$) scalar elliptic PDEs endowed with homogeneous essential boundary conditions. Their variational formulation reads as in Eq. (2.12) with $V \equiv H_0^m(\Omega) := \left\{ v \in H^m(\Omega) \ : \ \gamma_{\partial\Omega}^{(\iota)} v = 0 \text{ for } 0 \leq \iota \leq m-1 \right\}$, where $\gamma_{\partial\Omega}^{(\iota)}$ is the trace operator of order ι on $\partial\Omega$; see for reference [1].

We present the error estimates under h–refinement and, as in [3], we assume that the family of meshes $\{Q_h\}_h$ is generated under h–refinement starting from a coarsest mesh Q_{h_0} representing the computational domain. All the meshes are assumed to be (uniformly) shape regular and locally quasi–uniform [3]. Moreover, we define the NURBS space in the physical domain Ω, $\mathcal{V}^h$, by means of NURBS basis functions of degree $p_\alpha \equiv p$ for all $\alpha = 1, \ldots, d = \kappa$.

In the following, we will generically denote with C_{shape} a positive constant independent of the mesh size h and the unknown solution u of problem (2.12), but dependent on the shape of the domain Ω and its parametrization.

3.1 The interpolation error estimate for NURBS

We start by recalling some results concerning the interpolation theory of NURBS, as reported in [3]. The interpolation error estimate in norm H^m is based on the introduction of a *support extension* $\overline{Q}$ of an element Q of the mesh $\mathcal{Q}_h$ in the parametric domain, defined as the union of the supports of basis functions whose support intersect the element Q. Similarly, we define the *physical support estension* of an element $K = \mathbf{x}(Q)$ of the physical mesh $\mathcal{K}_h$ (2.10), as the image of $\overline{Q}$ through the geometrical mapping $\mathbf{x}$ (2.9) and we denote it as $\overline{K}$, i.e. $\overline{K} := \mathbf{x}(\overline{Q})$. Given a function $\widehat{v} \in L^2(\widehat{\Omega})$ defined in the parametric domain $\widehat{\Omega}$, we use the projective operator over the B–Splines space $\mathcal{S}_h$, say $\Pi_{\mathcal{S}_h}$, introduced in [3, 42] and defined as:

$$\Pi_{\mathcal{S}_h} : L^2(\widehat{\Omega}) \to \mathcal{S}_h, \qquad \Pi_{\mathcal{S}_h}\widehat{v} := \sum_{\boldsymbol{i}\in I} \lambda_{\boldsymbol{i}}(\widehat{v}) N_{\boldsymbol{i}}, \tag{3.1}$$

where the linear functionals $\lambda_{\boldsymbol{j}} \in L^2(\widehat{\Omega})'$ determine the dual basis for the set of B-Splines [42], i.e. they are such that $\lambda_{\boldsymbol{j}}(N_{\boldsymbol{i}}) := \delta_{\boldsymbol{j},\boldsymbol{i}}$ for $\boldsymbol{i}, \boldsymbol{j} \in I$. The corresponding projective operator over the NURBS space $\mathcal{N}_h$ in the parametric domain (2.8), say $\Pi_{\mathcal{N}_h}$, is defined by means of $\Pi_{\mathcal{S}_h}$ and the definition of the NURBS basis functions of (2.7) through the weighting function W of Eq. (2.6). In particular, $\Pi_{\mathcal{N}_h}$ reads:

$$\Pi_{\mathcal{N}_h} : L^2(\widehat{\Omega}) \to \mathcal{N}_h, \qquad \Pi_{\mathcal{N}_h}\widehat{v} := \frac{\Pi_{\mathcal{S}_h}(W\widehat{v})}{W}, \tag{3.2}$$

for all $\widehat{v} \in L^2(\widehat{\Omega})$. In this manner, the projective operator over $\mathcal{V}^h$, the NURBS space in the physical domain Ω defined in Eq. (2.11) as the push–forward of the space $\mathcal{N}_h$, is given by:

$$\Pi_{\mathcal{V}^h} : L^2(\Omega) \to \mathcal{V}^h, \qquad \Pi_{\mathcal{V}^h} v := (\Pi_{\mathcal{N}^h}(\widehat{v})) \circ \mathbf{x}^{-1}. \tag{3.3}$$

Firstly, we recall the estimate for the local interpolation error presented in [3]; then, we provide a global estimate taking into account the minimum global regularity of the basis functions $k_{\min}$.

Theorem 3.1 (Local interpolation error estimate)**.** *Given the integers l and s such that $0 \le l \le s \le p+1$ and $s \ge m$, for a function $u \in L^2(\Omega) \cap H^s(\overline{K})$, the estimate for the local interpolation error reads:*

$$|u - \Pi_{\mathcal{V}^h} u|_{H^l(K)} \le C_{shape}\, h_K^{s-l} \sum_{i=0}^{s} \|\nabla \mathbf{x}\|^{i-s}_{L^\infty(\overline{Q})} |u|_{H^i(\overline{K})}, \tag{3.4}$$

where h_K is the element size of $K \in \mathcal{K}_h$ and $\nabla\mathbf{x}$ denotes the deformation tensor of the geometrical mapping $\mathbf{x}$ provided in Eq. (2.9)*.*

By extending the results of [3] and using similar arguments, we provide the following result.

Proposition 3.1. *Given the integers l and s such that $0 \le l \le s \le p+1$ and $s \ge m$, and a function $u \in H^s(\Omega)$, then:*

$$\sum_{K\in\mathcal{K}_h} |u - \Pi_{\mathcal{V}^h} u|^2_{H^l(K)} \le C_{shape}\, h^{2(s-l)}\, \|u\|^2_{H^s(\Omega)}. \tag{3.5}$$

Proof. Firstly, we consider the local interpolation error estimate (3.4). By embedding the term related to the geometrical mapping ($\|\nabla\mathbf{x}\|_{L^\infty(\overline{Q})}$) into the constant C_{shape} and by elevating to the square, we obtain:

$$\begin{aligned} |u - \Pi_{\mathcal{V}^h} u|^2_{H^l(K)} &\le C_{\text{shape}}\, h_K^{2(s-l)} \left(\sum_{i=0}^{s} |u|_{H^i(\overline{K})} \right)^2 \le C_{\text{shape}}\, h_K^{2(s-l)} \left(\|u\|^2_{H^s(\overline{K})} + \sum_{i,j=0}^{s} |u|_{H^i(\overline{K})} |u|_{H^j(\overline{K})} \right) \\ &\le C_{\text{shape}}\, h_K^{2(s-l)} \|u\|^2_{H^s(\overline{K})}, \end{aligned} \tag{3.6}$$

where the third inequality holds since $|u|_{H^j(\overline{K})} \le \|u\|_{H^s(\overline{K})}$ for all $j = 0, \ldots, s$ and having included the term $(s+1)^2 + 1$ into the last of the constants C_{shape}. By summing the terms in inequality (3.6) over all the elements K in the physical mesh $\mathcal{K}_h$, we deduce from Eq. (3.6):

$$\sum_{K\in\mathcal{K}_h} |u - \Pi_{\mathcal{V}^h} u|^2_{H^l(K)} \le \sum_{K\in\mathcal{K}_h} C_{\text{shape}}\, h_K^{2(s-l)} \|u\|^2_{H^s(\overline{K})} \le C_{\text{shape}}\, h^{2(s-l)} \sum_{K\in\mathcal{K}_h} \sum_{K'\in\overline{K}} \|u\|^2_{H^s(K')}. \tag{3.7}$$

For each element $K \in \mathcal{K}_h$ we define a constant $\widetilde{E}_K$ equal to the number of support extensions to which K belongs. Due to the property of compact supports of the NURBS basis functions (for which the supports are the union of a finite set of elements, whose cardinality is bounded by the degree p and the dimension d of the parametric domain $\widehat{\Omega}$), there exists a constant $\widetilde{E}$ such that $\widetilde{E} \geq \max_{K \in \mathcal{K}_h} \widetilde{E}_K$, with $\widetilde{E}$ depending only on the degree p and the dimension d of the parametric domain. In this manner, the double sum in the last inequality of Eq. (3.7) is bounded as $\sum_{K \in \mathcal{K}_h} \sum_{K' \in \overline{K}} \|u\|^2_{H^s(K')} \leq \widetilde{E} \sum_{K \in \mathcal{K}_h} \|u\|^2_{H^s(K)}$. Then, by embedding the constant $\widetilde{E}$ in C_{shape}, we obtain:

$$\sum_{K \in \mathcal{K}_h} |u - \Pi_{\mathcal{V}^h} u|^2_{H^l(K)} \leq C_{\text{shape}}\, h^{2(s-l)} \sum_{K \in \mathcal{K}_h} \|u\|^2_{H^s(K)}, \tag{3.8}$$

from which the estimate (3.5) follows. □

Proposition 3.2 (Global interpolation error estimate)**.** *Under the hypotheses of Proposition 3.1, if in addition we have* $l \leq k_{\min}$*, we obtain:*

$$|u - \Pi_{\mathcal{V}^h} u|_{H^l(\Omega)} \leq C h^{s-l} \|u\|_{H^s(\Omega)}. \tag{3.9}$$

Proof. Under the additional hypothesis $l \leq k_{\min}$, the semi–norm in $H^l(\Omega)$ of the interpolation error $(u - \Pi_{\mathcal{V}^h} u)$ is well-defined on the whole space Ω and the result (3.9) follows from Eq. (3.5). □

Corollary 3.1. *Let* $u \in H^r(\Omega)$ *be a function defined in the physical domain* Ω*. Given an integer* l *such that* $0 \leq l \leq p+1$*,* $l \leq r$*, and* $l \leq k_{min}$*, then:*

$$|u - \Pi_{\mathcal{V}^h} u|_{H^l(\Omega)} \leq C h^{\delta-l} \|u\|_{H^r(\Omega)}. \tag{3.10}$$

where $\delta := \min\{r, p+1\}$*.*

Proof. By assuming $u \in H^r(\Omega)$, the estimate (3.10) follows directly from Proposition 3.2 and from the Sobolev inclusions $H^r(\Omega) \subseteq H^s(\Omega)$ for $r > s$. Indeed, if $r \leq p+1$ the hypotheses of Proposition 3.2 are satisfied by taking $s = r$ and δ equals r, while if $r \geq p+1$ the larger s satisfying the hypotheses in Proposition 3.2 is $s = p+1$ and we have $\delta = p+1$. □

Remark 3.1. *The approximation results of Propositions 3.1, 3.2 and Corollary 3.1 highlight the dependence of the error on the mesh size* h*, considering the family of meshes undergoing the* h*–refinement procedure. The explicit dependence of the interpolation error on the degree* p *and on the global regularity of the basis, expressed in terms of the smoothness integer parameter defining the vector* $\mathcal{K}$*, is provided in [6]. However, the results presented therein are obtained under more restricting hypotheses.*

3.2 A priori error estimate

We provide the error estimate for NURBS–based IGA in the H^m norm for elliptic PDEs of order $2m$, with $m \geq 1$. The result extends the one provided in [3] for second order PDEs.

Theorem 3.2 (A priori error estimate in norm H^m)**.** *Let* $u \in H^r(\Omega)$ *be the exact solution of problem* (2.12) *and* $u_h \in V^h$ *the approximate solution obtained with the NURBS–based IGA method with basis functions of global regularity* $k_{\min} \geq m$*. Then, the following* a priori *error estimate holds:*

$$\|u - u_h\|_{H^m(\Omega)} \leq C_{shape}\, h^{\gamma} \|u\|_{H^r(\Omega)}, \tag{3.11}$$

where $\gamma := \min\{p+1,\ r\} - m$*.*

Proof. By means of the optimal error estimate (2.16) of Theorem 2.1 and the approximation result (3.10) of Corollary 3.1, we have:

$$\begin{aligned}\|u-u_h\|_{H^m(\Omega)} &\leq \frac{M}{\alpha_c}\inf_{v_h\in V^h}\|u-v_h\|_{H^m(\Omega)} \leq C_{\text{shape}}\,\|u-\Pi_{\mathcal{V}^h}u\|_{H^m(\Omega)} \\ &\leq C_{\text{shape}}\,|u-\Pi_{\mathcal{V}^h}u|_{H^m(\Omega)} \leq C_{\text{shape}}\,h^{\min\{r,p+1\}-m}\|u\|_{H^r(\Omega)}.\end{aligned} \tag{3.12}$$

The third inequality is the generalization of *Poincaré inequality*, being the domain Ω bounded and featuring a regular boundary $\partial\Omega$; see for reference Corollary 6.31 in [1]. Then, the result (3.11) follows by definition of γ. □

In order to derive error estimates in lower order norms of the NURBS–based IGA approximation, we use arguments similar to those typically applied for the FEA; see e.g. [35, 40, 43]. In particular, we consider the Aubin–Nietsche's argument by introducing the adjoint problem and we use a generalized form of the *Lax–Milgram Lemma*, namely the *Nečas–Babuška Theorem*; see, e.g., [35, 41, 43].

Theorem 3.3 (A priori error estimate in lower order norms)**.** *For the elliptic PDE of order* $2m$ (2.12)*, with* $m\geq 1$*, let* σ *be an integer such that* $0\leq\sigma\leq m$ *and the linear functional* $F\in H^{-\sigma}(\Omega)$*. Let* $u\in H^r(\Omega)$*, with* $r\geq m$*, be the exact solution of problem* (2.12) *and* u_h *the approximate solution obtained with NURBS–based IGA with basis functions of degree* p*, and* $k_{min}\geq m$*. Then, the following a priori error estimate holds:*

$$\|u-u_h\|_{H^\sigma(\Omega)} \leq C_{shape}\,h^{\beta}\|u\|_{H^r(\Omega)}, \tag{3.13}$$

where $\beta:=\min\{\delta-\sigma,\ 2(\delta-m)\}$ *with* $\delta:=\min\{r,p+1\}$*.*

Proof. The *adjoint problem* associated with problem (2.12) and functional $F(\cdot)$, reads:

$$\text{find } \varphi_F\in V \quad : \quad a^*(\varphi_F,v)=F(v) \quad \forall v\in V, \tag{3.14}$$

where the bilinear form $a^*:V\times V\to\mathbb{R}$ is defined as $a^*(v,w):=a(w,v)$ for all $w,v\in V$ (see for instance [29, 35, 40]). The elliptic regularity of the adjoint problem follows from problem (2.12). Moreover, by means of the space embedding rule $V\subseteq H^\sigma\subseteq H^{-\sigma}\subseteq V'$ and the hypothesis $F\in H^{-\sigma}(\Omega)$, the adjoint problem (3.14) satisfies the hypotheses of the Nečas–Babuška Theorem [35, 41, 43]; thus, there exists a unique solution $\varphi_F\in V$ of the adjoint problem (3.14) and $\|\varphi_F\|_{H^{2m-\sigma}(\Omega)}\leq\widetilde{C}\|F\|_{H^{-\sigma}(\Omega)}$, for some constant $\widetilde{C}$ dependent on the weakly coerciveness of $a(\cdot,\cdot)$. By means of the generalized *Poincaré inequality* and the approximation result of Corollary 3.1, there exists a projection operator $\Pi_{\mathcal{V}^h}$ (see Eq. (3.3)) onto the NURBS space $\mathcal{V}^h$, for which:

$$\|\varphi_F-\Pi_{\mathcal{V}^h}\varphi_F\|_{H^m(\Omega)}\leq Ch^{\theta}\|\varphi_F\|_{H^{2m-\sigma}(\Omega)}, \tag{3.15}$$

with C a positive constant independent of the mesh size h, but dependent on the shape of the domain Ω and θ defined as:

$$\theta:=\begin{cases}\min\{m-\sigma,p+1-m\} & \text{if } r\geq 2m-\sigma,\\ \min\{r-m,p+1-m\} & \text{if } r<2m-\sigma.\end{cases} \tag{3.16}$$

The inequality (3.15) follows by considering, for the case $r\geq 2m-\sigma$, $\varphi_F\in H^r(\Omega)$ as an element of $H^{2m-\sigma}(\Omega)$ in virtue of the inclusion $H^r(\Omega)\subseteq H^{2m-\sigma}(\Omega)$, while for $r<2m-\sigma$ we simply observe that $\|\varphi_F\|_{H^r(\Omega)}\leq\|\varphi_F\|_{H^{2m-\sigma}(\Omega)}$.

By definition of the H^σ norm and by choosing $v=u-u_h$ in Eq. (3.14), we have:

$$\|u-u_h\|_{H^\sigma(\Omega)}=\sup_{F\in H^{-\sigma}(\Omega)}\frac{|\langle F,\ u-u_h\rangle_{H^{-\sigma}(\Omega),H^\sigma(\Omega)}|}{\|F\|_{H^{-\sigma}(\Omega)}}=\sup_{F\in H^{-\sigma}(\Omega)}\frac{|a^*(\varphi_F,\ u-u_h)|}{\|F\|_{H^{-\sigma}(\Omega)}}.$$

By means of the Galerkin orthogonality of the error with respect to $\mathcal{V}^h$ and the continuity of the bilinear form $a^*(\cdot,\cdot)$, we obtain:

$$\begin{aligned} \|u-u_h\|_{H^\sigma(\Omega)} &= \sup_{F\in H^{-\sigma}(\Omega)} \frac{|a^*(\varphi_F-\Pi_{\mathcal{V}^h}\varphi_F,\, u-u_h)|}{\|F\|_{H^{-\sigma}(\Omega)}} \\ &\leq M\|u-u_h\|_{H^m(\Omega)} \sup_{F\in H^{-\sigma}(\Omega)} \frac{\|\varphi_F-\Pi_{\mathcal{V}^h}\varphi_F\|_{H^m(\Omega)}}{\|F\|_{H^{-\sigma}(\Omega)}}. \end{aligned} \tag{3.17}$$

Then, by applying the error estimate (3.11) of Theorem 3.2 and the upper bound (3.15), we have:

$$\|u-u_h\|_{H^\sigma(\Omega)} \leq C_{\text{shape}}\, h^{\gamma+\theta}\|u\|_{H^r(\Omega)} \sup_{F\in H^{-\sigma}} \frac{\|\varphi_F\|_{H^{2m-\sigma}(\Omega)}}{\|F\|_{H^{-\sigma}(\Omega)}}.$$

Finally, by considering the inequality $\|\varphi_F\|_{H^{2m-\sigma}(\Omega)} \leq \widetilde{C}\|F\|_{H^{-\sigma}(\Omega)}$ and summing the exponents of $h^{\gamma+\theta}$, we obtain the result (3.13). ☐

From Theorems 3.2 and 3.3, we deduce that the convergence rate of the error with respect to the global mesh size h depends on the order of problem m, the regularity r of the exact solution $u \in H^r(\Omega)$, and the degree p of the NURBS basis functions used to represent the approximate solution $u_h \in V^h$. Moreover, when considering the a priori error estimate in lower order norms, the rate of convergence β in Eq. (3.13) depends also on the norm $H^\sigma(\Omega)$ used for the estimation of the error $u-u_h$. We observe that the smaller is σ, the larger is the expected convergence rate of the error with the mesh size h, provided that p is large enough with respect to m for $u \in H^r(\Omega)$, with $r \geq p+1$. In fact, this consideration does not hold when using a degree $p \leq 2m-1$, for which we obtain that the rate of convergence β is constant and equal to $2(p+1-m)$ for all $\sigma \leq 2m-1-p$. For example, for $m=2$ we obtain that:

$$\begin{aligned} \|u-u_h\|_{L^2(\Omega)} &\leq Ch^{min\{p+1,\,2p-2\}}\|u\|_{H^r(\Omega)}, \\ \|u-u_h\|_{H^1(\Omega)} &\leq Ch^{min\{p,\,2p-2\}}\|u\|_{H^r(\Omega)}, \\ \|u-u_h\|_{H^2(\Omega)} &\leq Ch^{min\{p-1,\,2p-2\}}\|u\|_{H^r(\Omega)}. \end{aligned} \tag{3.18}$$

If $p=2$, the convergence rates for the errors in norms $L^2(\Omega)$ and $H^1(\Omega)$ are coincident and equal to 2. In the case $m=3$, we obtain:

$$\begin{aligned} \|u-u_h\|_{L^2(\Omega)} &\leq Ch^{min\{p+1,\,2p-4\}}\|u\|_{H^r(\Omega)}, \\ \|u-u_h\|_{H^1(\Omega)} &\leq Ch^{min\{p,\,2p-4\}}\|u\|_{H^r(\Omega)}, \\ \|u-u_h\|_{H^2(\Omega)} &\leq Ch^{min\{p-1,\,2p-4\}}\|u\|_{H^r(\Omega)}, \\ \|u-u_h\|_{H^3(\Omega)} &\leq Ch^{min\{p-2,\,2p-4\}}\|u\|_{H^r(\Omega)}. \end{aligned} \tag{3.19}$$

We conclude that, for $m=3$, the same convergence rates of the errors in low order norms are obtained up to the degree $p=4$; in fact, if $p=3$, the convergence rates for the errors in norms $L^2(\Omega)$, $H^1(\Omega)$ and $H^2(\Omega)$ are equal to 2, while if $p=4$, only the convergence rates in norms $L^2(\Omega)$ and $H^1(\Omega)$ are equal to 4.

4 Examples of high order PDEs

In this section we provide some examples of high order (fourth and sixth order) scalar elliptic PDEs and we consider the Navier–Stokes equations in stream function formulation (fourth order scalar PDEs). We recall the governing equations and the corresponding variational forms, which we will solve numerically by means of NURBS–based IGA in the framework of the Galerkin method. Moreover, in Section 4.1 we briefly discuss the strong imposition of essential boundary conditions for high order PDEs solved with the above specified method.

4.1 Strong imposition of essential boundary conditions and lifting functions

We consider the model problem:

$$\text{find } w:\Omega\to\mathbb{R} \quad : \quad \begin{cases} \mathcal{L}w = f & \text{in } \Omega, \qquad (4.1a)\\ \mathcal{B}_\iota^{\text{Ess}} w = g_{\iota+1} & \text{on } \partial\Omega \quad \text{for all } \iota = 0,\ldots,m-1, \qquad (4.1b)\end{cases}$$

where $\mathcal{L}$ is a scalar linear elliptic partial differential operator of order $2m$, with $m \geq 1$, and $\left\{\mathcal{B}_\iota^{\text{Ess}}\right\}_{\iota=0}^{m-1}$ is a set of essential boundary operators. Moreover, $g_{\iota+1}$ for $\iota = 0,\ldots,m-1$ and f are functions satisfying suitable regularity hypotheses; see [35]. We define the trial affine space $V_g := \left\{v \in H^m(\Omega) : \gamma_{\partial\Omega}^{(\iota)} v = g_{\iota+1} \text{ for } 0 \leq \iota \leq m-1\right\} \subset H^m(\Omega)$ (see [1]) and we introduce a lifting function $\bar{g} \in H^m(\Omega)$ satisfying all the essential boundary conditions (4.1b) in the sense of the traces, i.e. such that $\gamma_{\partial\Omega}^{(\iota)}\bar{g} = g_{\iota+1}$ for all $\iota = 0,\ldots,m-1$; see [1] and [31]. Moreover, $\bar{g}$ is such that for all functions $w \in V_g$ there exists a unique $u \in V \equiv H_0^m(\Omega)$ for which $w = \bar{g} + u$. In this manner, we recast problem (4.1) in the weak formulation (2.12) by introducing a bilinear form $a : V \times V \to \mathbb{R}$ corresponding to the differential operator $\mathcal{L}$ and a linear functional $F : V \to \mathbb{R}$ depending on the source term f and on the lifting function $\bar{g}$, i.e. such that $F(v) = \langle f,\, v\rangle_{L^2(\Omega)} - a(\bar{g}, v)$ for all test functions $v \in V$.

In view of the numerical approximation of problem (2.12) by means of NURBS–based IGA in the framework of the Galerkin method, we look for a numerical solution of problem (2.14), u_h belonging to the space $V^h = V \cap \mathcal{V}^h$, where $\mathcal{V}^h$ is the NURBS space (see Eq. (2.11)). If the functions $g_{\iota+1}$ for $\iota = 0,\ldots,m-1$ do not belong to a subspace of $\mathcal{V}^h$, say $\mathcal{V}^h_{\partial\Omega}$, defined as the space of the traces of the functions in $\mathcal{V}_h$ on $\partial\Omega$, we consider an approximation $g_{\iota+1,h} \approx g_{\iota+1}$ such that $g_{\iota+1,h} \in \mathcal{V}^h_{\partial\Omega}$ for each $\iota = 0,\ldots,m-1$, e.g. obtained by means of an L^2 projection technique onto the NURBS space $\mathcal{V}^h_{\partial\Omega}$. Once provided the set of functions $\{g_{\iota+1,h}\}_{\iota=0}^{m-1}$, we define the trial discrete affine space $V_g^h := \left\{v_h \in \mathcal{V}^h \ : \ \gamma_{\partial\Omega}^{(\iota)} v_h = g_{\iota+1,h} \ \text{ for } \ 0 \leq \iota \leq m-1\right\} \subset \mathcal{V}^h$, whose NURBS functions satisfy the discrete approximation of the essential boundary conditions (4.1b) in the sense of the traces. We observe that, if $g_{\iota+1} \in \mathcal{V}^h$ for all $\iota = 0,\ldots,m-1$ (i.e. if $g_{\iota+1,h} \equiv g_{\iota+1}$), we have $V_g^h \equiv V_g \cap \mathcal{V}^h$. Then, we introduce the approximate lifting function $\bar{g}_h \in V_g^h$ such that $\gamma_{\partial\Omega}^{(\iota)}\bar{g}_h = g_{\iota+1,h}$ for all $\iota = 0,\ldots,m-1$ and for all $w_h \in V_g^h$ there exists a unique $u_h \in V^h$ for which $w_h = \bar{g}_h + u_h$. In this manner, we can recast the discrete problem in the form of Eq. (2.14), where the linear functional $F(\cdot)$ is replaced by $F_h : V^h \to \mathbb{R}$, which includes the term associated to the discrete lifting function, i.e. $F_h(v_h) = \langle f,\, v_h\rangle_{L^2(\Omega)} - a(\bar{g}_h, v_h)$ for all test functions $v_h \in V^h$.

We recall that the strong imposition of the essential boundary conditions (4.1b), or possibly their approximation in terms of the functions $g_{\iota+1,h}$, is facilitated in the NURBS framework. Indeed, due to the locality and the tensor product construction of the NURBS basis functions, the m homogeneous essential boundary conditions are enforced simply by setting equal to zero the m outermost control variables along the parametric direction normal to the boundary $\partial\Omega$. Similarly, the lifting function $\bar{g}_h \in V_g^h$ is determined by setting the values of the same m outermost control variables accordingly with the functions $g_{\iota+1,h}$ for all $\iota = 0,\ldots,m-1$ and the other control variables equal to zero. For more details and an extensive overview of the topic, we refer the reader to [19, 32, 44].

4.2 Biharmonic and Triharmonic problems

The biharmonic problem is governed by a fourth order partial differential operator $\triangle^2 := \triangle\triangle$, often called *bilaplacian.* Since we restrict to the case of essential boundary conditions on the whole boundary $\partial\Omega$, the problem in strong form reads:

$$\text{find } w:\Omega\to\mathbb{R} \quad : \quad \begin{cases} \triangle^2 w = f & \text{in } \Omega, \qquad (4.2a)\\ w = g_1 & \text{on } \partial\Omega, \qquad (4.2b)\\ \nabla w \cdot \mathbf{n} = g_2 & \text{on } \partial\Omega. \qquad (4.2c)\end{cases}$$

We define the trial and test function spaces as, respectively:

$$V_g = \left\{ v \in H^2(\Omega) \ : \ \gamma^{(0)}_{\partial\Omega} v = v|_{\partial\Omega} = g_1, \quad \gamma^{(1)}_{\partial\Omega} v = (\nabla v \cdot \mathbf{n})|_{\partial\Omega} = g_2 \right\}, \tag{4.3a}$$

$$V = \left\{ v \in H^2(\Omega) \ : \ \gamma^{(0)}_{\partial\Omega} v = v|_{\partial\Omega} = 0, \quad \gamma^{(1)}_{\partial\Omega} v = (\nabla v \cdot \mathbf{n})|_{\partial\Omega} = 0 \right\}. \tag{4.3b}$$

We consider a suitable lifting function $\bar{g} \in H^2(\Omega)$ satisfying the essential boundary conditions (4.2b–4.2c) in the sense of the traces, i.e. such that $\gamma^{(0)}_{\partial\Omega}\bar{g} = \bar{g}|_{\partial\Omega} = g_1$ and $\gamma^{(1)}_{\partial\Omega}\bar{g} = (\nabla\bar{g}\cdot\mathbf{n})|_{\partial\Omega} = g_2$. In this manner, we recast problem (4.2) in the weak formulation (2.12) in terms of the unknown $u \in V \equiv H^2_0(\Omega)$ such that $w = \bar{g} + u$, with the bilinear form $a(u,v) := \int_\Omega \triangle u \triangle v \, d\Omega$ and the linear functional $F(v) := \int_\Omega f v \, d\Omega - a(\bar{g}, v)$. Following the procedure described in Section 4.1, the discrete counterpart of problem (2.12) reads as in Eq. (2.14) in the unknown function $u_h \in V^h$. By considering the differentiability requirements on the unknown $u_h \in V^h$ and test functions, the numerical approximation by means of the Galerkin method requires that the NURBS space $\mathcal{V}^h$ must be defined by means of basis functions which are at least globally $\mathcal{C}^1$–continuous.

The triharmonic problem is governed by the sixth order partial differential operator $\triangle^3 := \triangle\triangle^2$, called *trilaplacian*; if complemented by essential boundary conditions on the whole boundary $\partial\Omega$, it reads:

$$\text{find } w : \Omega \to \mathbb{R} \quad : \quad \begin{cases} -\triangle^3 w = f & \text{in } \Omega, & (4.4a) \\ w = g_1 & \text{on } \partial\Omega, & (4.4b) \\ \nabla w \cdot \mathbf{n} = g_2 & \text{on } \partial\Omega, & (4.4c) \\ \triangle w = g_3 & \text{on } \partial\Omega. & (4.4d) \end{cases}$$

Problems involving a sixth order partial differential operator arise e.g. in phase field crystal models [28], geometrical PDEs for surface modeling [33], and fracture modeling [46].

In order to provide the variational formulation of problem (4.4), we define the trial and test function spaces as:

$$V_g = \left\{ v \in H^3(\Omega) \ : \ \gamma^{(0)}_{\partial\Omega} v = v|_{\partial\Omega} = g_1, \quad \gamma^{(1)}_{\partial\Omega} v = (\nabla v \cdot \mathbf{n})|_{\partial\Omega} = g_2, \quad \gamma^{(2)}_{\partial\Omega} v = \triangle v|_{\partial\Omega} = g_3 \right\}, \tag{4.5a}$$

$$V = \left\{ v \in H^3(\Omega) \ : \ \gamma^{(0)}_{\partial\Omega} v = v|_{\partial\Omega} = 0, \quad \gamma^{(1)}_{\partial\Omega} v = (\nabla v \cdot \mathbf{n})|_{\partial\Omega} = 0, \quad \gamma^{(2)}_{\partial\Omega} v = \triangle v|_{\partial\Omega} = 0 \right\}, \tag{4.5b}$$

respectively. We consider a suitable lifting function $\bar{g} \in H^3(\Omega)$ satisfying the essential boundary conditions (4.4b–4.4d) in the sense of the traces, i.e. such that $\gamma^{(0)}_{\partial\Omega}\bar{g} = \bar{g}|_{\partial\Omega} = g_1$, $\gamma^{(1)}_{\partial\Omega}\bar{g} = (\nabla\bar{g}\cdot\mathbf{n})|_{\partial\Omega} = g_2$, and $\gamma^{(2)}_{\partial\Omega}\bar{g} = \triangle\bar{g}|_{\partial\Omega} = g_3$. In this manner, we recast problem (4.4) in the weak formulation (2.12) in terms of the unknown $u \in V \equiv H^3_0(\Omega)$ such that $w = \bar{g} + u$, where the bilinear form is given by $a(u,v) := \int_\Omega \nabla(\triangle u) \cdot \nabla(\triangle v) \, d\Omega$ and the linear functional is $F(v) := \int_\Omega f v \, d\Omega - a(\bar{g}, v)$. Following Section 4.1, the numerical approximation of problem (4.4) reads as in Eq. (2.14) with $u_h \in V^h$ being the unknown approximate solution. As already discussed in Remark 2.2, by considering the differentiability requirements on the unknown $u_h \in V^h$ and test functions, the numerical approximation by means of the NURBS–based IGA–Galerkin method applied to problem (4.4) requires that the NURBS space $\mathcal{V}^h$ must be defined by means of basis functions which are at least globally $\mathcal{C}^2$–continuous in Ω.

4.3 Navier–Stokes equations

We consider the Navier–Stokes equations governing the flow of an incompressible fluid in a domain $\Omega \subset \mathbb{R}^2$ and in the time interval $(0, T)$. We recall the dimensionless strong form of the problem expressed in terms of the primitive variables velocity and pressure $(\boldsymbol{u}, p)$, which reads:

find $\boldsymbol{u} : \Omega \times (0,T) \to \mathbb{R}^2$ and $p : \Omega \times (0,T) \to \mathbb{R}$ such that:

$$\begin{cases} \dot{\boldsymbol{u}} + (\boldsymbol{u} \cdot \nabla)\, \boldsymbol{u} + \nabla p - 2\nabla \cdot \left(\dfrac{1}{\mathbb{R}e} D(\boldsymbol{u}) \right) = \boldsymbol{f} & \text{in } \Omega,\ t \in (0,T), \quad (4.6a) \\ \nabla \cdot \boldsymbol{u} = 0 & \text{in } \Omega,\ t \in (0,T), \quad (4.6b) \\ \boldsymbol{u}(0) = \boldsymbol{u}_0 & \text{in } \Omega, \quad (4.6c) \\ \boldsymbol{\sigma}_f \mathbf{n} = \boldsymbol{h} & \text{on } \Gamma_N,\ t \in (0,T), \quad (4.6d) \\ \boldsymbol{u} = \boldsymbol{g} & \text{on } \Gamma_D,\ t \in (0,T), \quad (4.6e) \end{cases}$$

where $\mathbb{R}e$ is the Reynolds number, $\boldsymbol{\sigma}_f = -p\mathrm{I} + 2\dfrac{1}{\mathbb{R}e} D(\boldsymbol{u})$ is the Cauchy stress tensor, with $D(\boldsymbol{u}) := \dfrac{(\nabla \boldsymbol{u} + \nabla \boldsymbol{u}^T)}{2}$ the strain tensor, and I the identity tensor. The vector field $\boldsymbol{f} : \Omega \times (0,T) \to \mathbb{R}^2$ indicates the *body forces* and $\boldsymbol{u}_0 : \Omega \to \mathbb{R}^2$ is the initial condition. Neumann (4.6d) and Dirichlet (4.6e) boundary conditions are provided in terms of the vector fields $\boldsymbol{h}$ and $\boldsymbol{g}$, defined on the subsets $\Gamma_N, \Gamma_D \subseteq \partial\Omega$, respectively, with $\overline{\Gamma_D \cup \Gamma_N} = \partial\Omega$ and $\overset{\circ}{\Gamma}_D \cap \overset{\circ}{\Gamma}_N = \emptyset$; $\mathbf{n}$ indicates the outward directed unit vector normal to Γ_N. Moreover, we denote by $\dot{\boldsymbol{u}} := \dfrac{\partial \boldsymbol{u}}{\partial t}$.

4.3.1 Navier–Stokes equations in stream function formulation

We briefly recall the *stream function formulation* of the Navier–Stokes equations; we follow the same approach described in [2] for the plane linear elasticity problem for a homogeneous isotropic incompressible material. Specifically, we start from the variational formulation of problem (4.6), by defining the trial and test function spaces as $V_g := \left\{ \boldsymbol{v} \in \left[H^1(\Omega)\right]^2 \ :\ \boldsymbol{v}|_{\Gamma_D} = \boldsymbol{g} \right\}$ (this is indeed an affine manifold), $V := \left\{ \boldsymbol{v} \in \left[H^1(\Omega)\right]^2 \ :\ \boldsymbol{v}|_{\Gamma_D} = \boldsymbol{0} \right\}$, and $Q := L^2(\Omega)$. We introduce the spaces of divergence–free functions, subsets of the corresponding spaces V_g and V, defined as $W_g := \{\boldsymbol{v} \in V_g \ :\ \nabla \cdot \boldsymbol{v} = 0\} \subset V_g$ and $W := \{\boldsymbol{v} \in V \ :\ \nabla \cdot \boldsymbol{v} = 0\} \subset V$, respectively. Then, the weak form of the Navier–Stokes equations reads:

find, for all $t \in (0,T)$, $\boldsymbol{u}(t) \in W_g$ such that:

$$\begin{cases} m(\dot{\boldsymbol{u}}(t), \boldsymbol{v}) + a(\boldsymbol{u}(t), \boldsymbol{v}) + c(\boldsymbol{u}(t), \boldsymbol{u}(t), \boldsymbol{v}) = F(\boldsymbol{v}) + H(\boldsymbol{v}) & \forall \boldsymbol{v} \in W, \quad (4.7a) \\ \boldsymbol{u}(0) = \boldsymbol{u}_0 & \text{in } \Omega, \quad (4.7b) \end{cases}$$

where $m(\dot{\boldsymbol{u}}, \boldsymbol{v}) := \int_\Omega \dot{\boldsymbol{u}} \cdot \boldsymbol{v} \, \mathrm{d}\Omega$, $a(\boldsymbol{u}, \boldsymbol{v}) := \dfrac{2}{\mathbb{R}e} \int_\Omega D(\boldsymbol{u}) : D(\boldsymbol{v}) \, \mathrm{d}\Omega$, $b(\boldsymbol{v}, p) := -\int_\Omega p \, \nabla \cdot \boldsymbol{v} \, \mathrm{d}\Omega$ and $c(\boldsymbol{w}, \boldsymbol{u}, \boldsymbol{v}) := \int_\Omega ((\boldsymbol{w} \cdot \nabla)\boldsymbol{u}) \cdot \boldsymbol{v} \, \mathrm{d}\Omega$, while $F(\boldsymbol{v}) := \int_\Omega \boldsymbol{f} \cdot \boldsymbol{v} \, \mathrm{d}\Omega$ and $H(\boldsymbol{v}) := \int_{\Gamma_N} \boldsymbol{h} \cdot \boldsymbol{v} \, \mathrm{d}\Gamma$.

Moreover, we consider over the space of scalar functions $H^2(\Omega)$ the equivalence relation $\sim$ for which $\varphi \sim \psi$ if and only if $\psi - \varphi \in \mathbb{R}$, for all $\varphi, \psi \in H^2(\Omega)$; the resulting quotient space of scalar functions in $H^2(\Omega)$ identified up to a constant is denoted by $X := \{[\varphi] : \varphi \in H^2(\Omega)\}$ [1]. In the additional hypothesis that Ω is a simply connected domain, for a given $\boldsymbol{v} \in W$ there exists a unique $\varphi \in X$ such that $\boldsymbol{v} = \mathbf{curl}\varphi$, where the partial differential operator **curl** of scalar fields is defined as:

$$\mathbf{curl} : X \to [H^1(\Omega)]^2, \quad \mathbf{curl}\varphi := \left(\frac{\partial \varphi}{\partial \mathrm{y}}, -\frac{\partial \varphi}{\partial \mathrm{x}} \right); \tag{4.8}$$

see for reference [2, 26]. In particular, the operator **curl** provides an isomorphism between the spaces W_g, W and the following spaces $\Phi_g := \{\psi \in X \ :\ \mathbf{curl}\psi|_{\Gamma_D} = \boldsymbol{g}\}$ and $\Phi := \{\varphi \in X \ :\ \mathbf{curl}\varphi|_{\Gamma_D} = \boldsymbol{0}\}$, respectively. In this manner, we can rewrite problem (4.7) in term of the scalar function $\psi \in \Phi_g$, called *stream function*,

---

[1] For the sake of simplicity, we identify each element of X with its equivalence class, i.e. $\varphi \in X$ is intended as $\varphi \in [\varphi]$, with $[\varphi] \in X$.

which reads:

find, for all $t \in (0,T)$, $\psi(t) \in \Phi_g$ such that:

$$\begin{cases} \bar{m}(\dot{\psi}(t),\varphi) + \bar{a}(\psi(t),\varphi) + \bar{c}(\psi(t),\psi(t),\varphi) = \bar{F}(\varphi) + \bar{H}(\varphi) & \forall \varphi \in \Phi, \qquad (4.9a) \\ \psi(0) = \psi_0 & \text{in } \Omega \ , \qquad (4.9b) \end{cases}$$

where $\bar{m}(\dot{\psi},\varphi) := \int_\Omega \mathbf{curl}\dot{\psi} \cdot \mathbf{curl}\varphi \, d\Omega$, $\bar{a}(\psi,\varphi) := \frac{2}{\mathbb{R}e} \int_\Omega D(\mathbf{curl}\psi) : D(\mathbf{curl}\varphi) \, d\Omega$, $\bar{c}(\psi,\psi,\varphi) := \int_\Omega \big((\mathbf{curl}\psi \cdot \nabla)\mathbf{curl}\psi\big) \cdot \mathbf{curl}\varphi \, d\Omega$, $\bar{F}(\varphi) := \int_\Omega \boldsymbol{f} \cdot \mathbf{curl}\varphi \, d\Omega$, $\bar{H}(\varphi) := \int_{\Gamma_N} \boldsymbol{h} \cdot \mathbf{curl}\varphi \, d\Gamma$. The initial condition (4.9b) is chosen in such a way that $\mathbf{curl}\psi_0 = \boldsymbol{u}_0$. Problem (4.9) is the *stream function formulation* of the Navier–Stokes equations (4.6) and it represents a time dependent fourth order nonlinear PDE. By construction, $\boldsymbol{u} = \mathbf{curl}\psi$ is the velocity field solving problem (4.7) and it is, by definition, divergence free. The pressure field, unknown in Eq. (4.6), can be recovered by solving a second order PDE depending on the stream function ψ [26].

Remark 4.1. *By definition of the spaces Φ_g and Φ, the scalar field $\psi \in \Phi_g$ solution of problem* (4.9) *is not strictly a scalar function, but a class of equivalence of functions determined up to a constant. We enforce the uniqueness of the solution of problem* (4.9) *in a classical sense e.g. by enforcing a prescribed value in a point in the domain. Moreover, we recast the essential boundary condition* $(\mathbf{curl}\psi)\,|_{\Gamma_D} = \boldsymbol{g}$ *in the form of essential boundary conditions for fourth order PDEs, i.e. given $d_1, d_2 : \Gamma_D \to \mathbb{R}$, we set $\psi|_{\Gamma_D} = d_1$, $\nabla\psi \cdot \boldsymbol{n}|_{\Gamma_D} = d_2$. In particular, by means of the relation $\boldsymbol{curl}\psi = \boldsymbol{u}$, a Dirichlet boundary condition $\boldsymbol{u}|_{\Gamma_D} = \boldsymbol{g} = (g_\text{x}, g_\text{y})$ yields a condition of the form $\nabla\psi \cdot \boldsymbol{n}|_{\Gamma_D} = (-g_\text{y}, g_\text{x}) \cdot \boldsymbol{n}$. Moreover, by means of the fundamental theorem of calculus [38], the data d_1 associated to the essential boundary condition of zero order for the stream function ψ ($\psi|_{\Gamma_D} = d_1$) can be deduced from the set of boundary conditions for primitive variables.*

4.3.2 Navier–Stokes equations: numerical approximation

We provide the semi-discretized spatial approximation of problem (4.9) by means of the NURBS-based IGA–Galerkin method presented in Section 2.2. Moreover, we use the generalized–α method [14, 30] for the approximation in time.

Let the two–dimensional computational domain Ω be represented by a NURBS geometry. We consider the finite dimensional space of NURBS in the physical domain, say $\mathcal{V}^h$, given in Eq. (2.11) and we define the finite dimensional subspaces of the trial and test function spaces Φ_g and Φ as the NURBS spaces given respectively by $\Phi^h := \Phi \cap \mathcal{V}^h$ and $\Phi_g^h := \Phi_g \cap \mathcal{V}^h$, with $N_s := \dim \Phi^h$ the dimension and $\{\mathcal{R}_i\}_{i=1}^{N_s}$ the set of NURBS basis functions of Φ^h, respectively. The IGA–Galerkin approximation of problem (4.9) reads:

find, for all $t \in (0,T)$, $\psi_h(t) \in \Phi_g^h$ such that:

$$\begin{cases} \bar{m}(\dot{\psi}_h(t),\varphi_h) + \bar{a}(\psi_h(t),\varphi_h) + \bar{c}(\psi_h(t),\psi_h(t),\varphi_h) = \bar{F}(\varphi_h) + \bar{H}(\varphi_h) & \forall \varphi_h \in \Phi^h, \qquad (4.10a) \\ \psi_h(0) = \psi_0 & \text{in } \Omega, \qquad (4.10b) \end{cases}$$

where the forms and the functionals are the same used for problem (4.9). In view of the discretization in time, we rewrite Eq. (4.10a) in residual form as:

find, for all $t \in (0,T)$, $\psi_h(t) \in \Phi_g^h$ such that:

$$\begin{cases} R_h(\varphi_h, \dot{\psi}_h(t), \psi_h(t)) = 0 & \forall \varphi_h \in \Phi^h, \qquad (4.11a) \\ \psi_h(0) = \psi_0 & \text{in } \Omega, \qquad (4.11b) \end{cases}$$

with $R_h(\varphi_h, \dot{\psi}_h, \psi_h) := \bar{m}(\dot{\psi}_h, \varphi_h) + \bar{a}(\psi_h, \varphi_h) + \bar{c}(\psi_h, \psi_h, \varphi_h) - \bar{F}(\varphi_h) - \bar{H}(\varphi_h)$; we define the vector of discrete residuals whose components are the residuals $R_h(\cdot, \dot{\psi}_h, \psi_h)$ evaluated in the NURBS basis functions for the function space Φ^h ($\mathcal{R}_i$, for $i = 1, \ldots, N_s$), i.e. $\boldsymbol{R}\left(\dot{\psi}_h(t),\, \psi_h(t)\right) := \left\{R_h(\mathcal{R}_i;\, \dot{\psi}_h(t),\, \psi_h(t))\right\}_{i=1}^{N_s}$ for

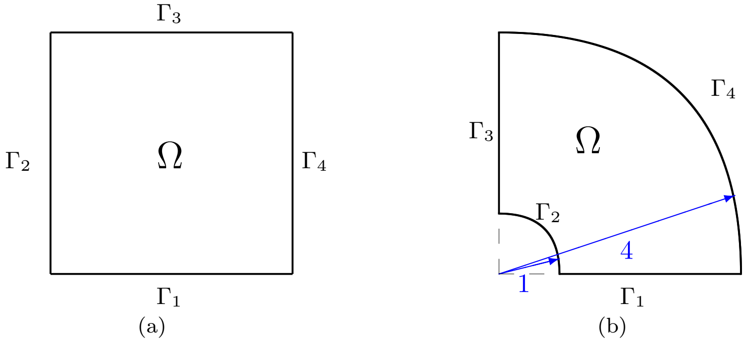

Figure 2: Computational domains: a square $\Omega = (0,1)^2$ (a) and a quarter of an annulus, $\Omega = (1,4) \times \left(0, \frac{\pi}{2}\right)$ in radial coordinates (b).

all $t \in (0,T)$. Moreover, we introduce the vectors of control variables for all $t \in (0,T)$ for the *function* ψ_h and its time derivative $\dot{\psi}_h$, given by $\dot{\boldsymbol{\Psi}}(t) = \left\{\dot{\psi}_i(t)\right\}_{i=1}^{N_s}$ and $\boldsymbol{\Psi}(t) = \left\{\psi_i(t)\right\}_{i=1}^{N_s}$, respectively. We define a *discrete time vector* $\{t_n\}_{n=0}^{N_t}$, subdividing $(0,T)$ in a set of N_t time intervals of size $\Delta t_n = t_{n+1} - t_n$; for the sake of simplicity, we replace the evaluation in t_n with the subscript n in the vectors of control variables.

In this framework, we perform the discretization in time by means of the generalized–α method (see [14, 30]): at time step t_n, given $\dot{\boldsymbol{\Psi}}_n$, $\boldsymbol{\Psi}_n$, find $\dot{\boldsymbol{\Psi}}_{n+1}$, $\boldsymbol{\Psi}_{n+1}$, $\dot{\boldsymbol{\Psi}}_{n+\alpha_m}$, $\boldsymbol{\Psi}_{n+\alpha_f}$ such that:

$$\boldsymbol{R}\left(\dot{\boldsymbol{\Psi}}_{n+\alpha_m},\, \boldsymbol{\Psi}_{n+\alpha_f}\right) = \boldsymbol{0}, \tag{4.12a}$$

$$\dot{\boldsymbol{\Psi}}_{n+\alpha_m} = \dot{\boldsymbol{\Psi}}_n + \alpha_m \left(\dot{\boldsymbol{\Psi}}_{n+1} - \dot{\boldsymbol{\Psi}}_n\right), \tag{4.12b}$$

$$\boldsymbol{\Psi}_{n+\alpha_f} = \boldsymbol{\Psi}_n + \alpha_f \left(\boldsymbol{\Psi}_{n+1} - \boldsymbol{\Psi}_n\right), \tag{4.12c}$$

$$\boldsymbol{\Psi}_{n+1} = \boldsymbol{\Psi}_n + \Delta t_n \dot{\boldsymbol{\Psi}}_n + \delta \Delta t_n \left(\dot{\boldsymbol{\Psi}}_{n+1} - \dot{\boldsymbol{\Psi}}_n\right), \tag{4.12d}$$

where the parameters α_m, α_f, $\delta \in \mathbb{R}_0^+$ defining the generalized–α method, are chosen on the basis of accuracy and stability considerations; see [14, 30, 32]. Moreover, we deal with the nonlinearity of the system of equations (4.12) by using a *predictor–multicorrector algorithm* as done e.g. in [32].

5 Numerical results

We solve by means of NURBS–based IGA the high order PDEs described in Section 4, for which we verify the convergence rates predicted by the a priori error estimate of Eq. (3.13). Then, we solve the Navier–Stokes equations in stream function formulation for the benchmark lid–driven cavity problem; we compare the results with those available in literature, namely [10, 22] and [25].

5.1 High order elliptic PDEs: biharmonic and triharmonic problems

We consider two tests for the biharmonic problem (4.2) and an example for the triharmonic problem (4.4) for which the exact smooth solution is known. The problems are defined in the physical domains $\Omega \subset \mathbb{R}^2$ described in Figure 2 with homogeneous essential boundary conditions on the whole boundary $\partial\Omega \equiv \Gamma_1 \cup \Gamma_2 \cup \Gamma_3 \cup \Gamma_4$.

5.1.1 Biharmonic Problem

Case 1. By referring to Eq. (4.2), we consider a problem defined in the domain $\Omega = (0,1)^2$ as given in Figure 2a. In particular, we set $g_1(\mathrm{x},\mathrm{y}) = g_2(\mathrm{x},\mathrm{y}) = 0$ and the source term $f(\mathrm{x},\mathrm{y})$ yielding the exact

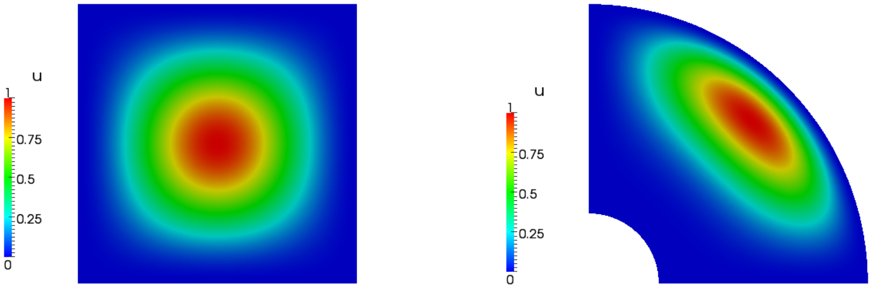

(a) *case 1* (b) *case 2*

Figure 3: Biharmonic problem: exact solutions of problems described in case 1 (a) and case 2 (b).

solution $u(\mathrm{x},\mathrm{y}) = \sin^2(\pi\mathrm{x})\sin^2(\pi\mathrm{y})$. The domain Ω is described by B–Splines on uniform meshes with a total number of elements $\mathrm{N}_{el} = \left(2^N\right)^2$, for which $h = \dfrac{1}{2^N}$ with $N = 2, \dots, 6$; we consider different choices of degree of the basis, namely $p = 2$, 3 and 4, yielding globally $\mathcal{C}^1$, $\mathcal{C}^2$ and $\mathcal{C}^3$–continuous basis functions, respectively. The hypotheses in Theorem 3.3 are satisfied for each degree p. In Figure 3a we show the exact solution u and in Figure 4 the convergence rates of the errors in norms L^2, H^1 and H^2 vs. the mesh size h. The comparison with the theoretical convergence rates numerically validate the a priori error estimate provided in Theorem 3.3. Moreover, by looking at Figure 4a, we observe that the considerations highlighted in Eq. (3.18) for $m = 2$ and $p = 2$ hold, leading the convergence rates for the errors in norms $L^2(\Omega)$ and $H^1(\Omega)$ both equal to 2.

Case 2. We consider the biharmonic problem (4.2) defined in the domain Ω represented by a quarter of an annulus with inner radius $r_{\mathrm{in}} = 1$ and outer radius $r_{\mathrm{out}} = 4$ as depicted in Figure 2b. The computational domain is exactly represented by means of NURBS basis function. In particular, we consider two different choices of degree of the basis, namely $p = 2$ and 3, and define uniform meshes with number of elements $\mathrm{N}_{el} = \left(2^N\right)^2$, where $N = 2, \dots, 6$ for $p = 2$, while $N = 2, \dots, 5$ for $p = 3$. The global mesh size h is represented in terms of the characteristic length of Ω, i.e. $H = \sqrt{\dfrac{\pi}{4}\left(r_{\mathrm{out}}^2 - r_{\mathrm{in}}^2\right)}$, and reads $h = \dfrac{H}{2^N}$ for each N. Then, problem (4.2) is defined by setting $g_1(\mathrm{x},\mathrm{y}) = g_2(\mathrm{x},\mathrm{y}) = 0$ on the whole boundary $\partial\Omega$ and the source term $f(\mathrm{x},\mathrm{y})$ yielding the exact solution $u(\mathrm{x},\mathrm{y}) = \dfrac{1}{\varsigma}\mathrm{x}^2\mathrm{y}^2\left(\mathrm{x}^2+\mathrm{y}^2-r_{\mathrm{in}}^2\right)^2\left(\mathrm{x}^2+\mathrm{y}^2-r_{\mathrm{out}}^2\right)^2$, with $\varsigma \in \mathbb{R}$ such that $\|u\|_{L^\infty(\Omega)} = 1$. In Figure 5 we show the convergence rates of the errors vs. the mesh size h, from which we observe that the theoretical convergence rates expected from Theorem 3.3 are confirmed.

5.1.2 Triharmonic Problem

We consider the triharmonic problem (4.4), for which we set homogeneous essential boundary conditions on the whole boundary $\partial\Omega$ ($g_1(\mathrm{x},\mathrm{y}) = g_2(\mathrm{x},\mathrm{y}) = g_3(\mathrm{x},\mathrm{y}) = 0$), and the source term $f(\mathrm{x},\mathrm{y})$ such that the exact smooth solution is $u(\mathrm{x},\mathrm{y}) = \sin^3(\pi\mathrm{x})\sin^3(\pi\mathrm{y})$. The problem is solved on k–refined uniform meshes with number of elements $\mathrm{N}_{el} = \left(2^N\right)^2$, for $N = 3, \dots, 7$, and for the degrees $p = 3$ and 4, yielding basis functions which are globally $\mathcal{C}^{p-1}$–continuous. The hypotheses in Theorem 3.3 are satisfied and the plots of errors vs. the mesh size h in Figure 6 confirm the theoretical results provided in Eq. (3.13). As reported in Eq. (3.19), we observe that for $p = 3$ the convergence rates of the errors in norms L^2, H^1, and H^2 are equal to 2. For $p = 4$ the convergence rates of the errors in norms L^2 and H^1 are instead equal to 4, as expected from Theorem 3.3.

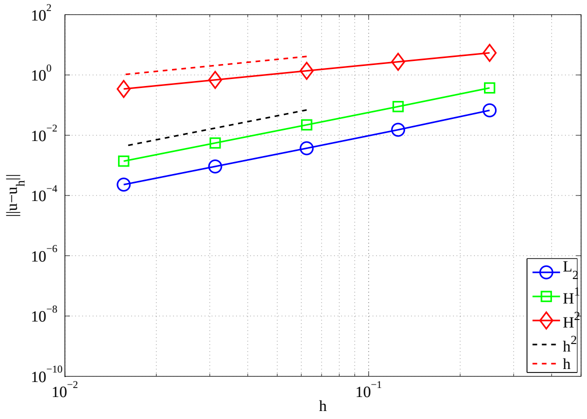

(a) $p = 2$.

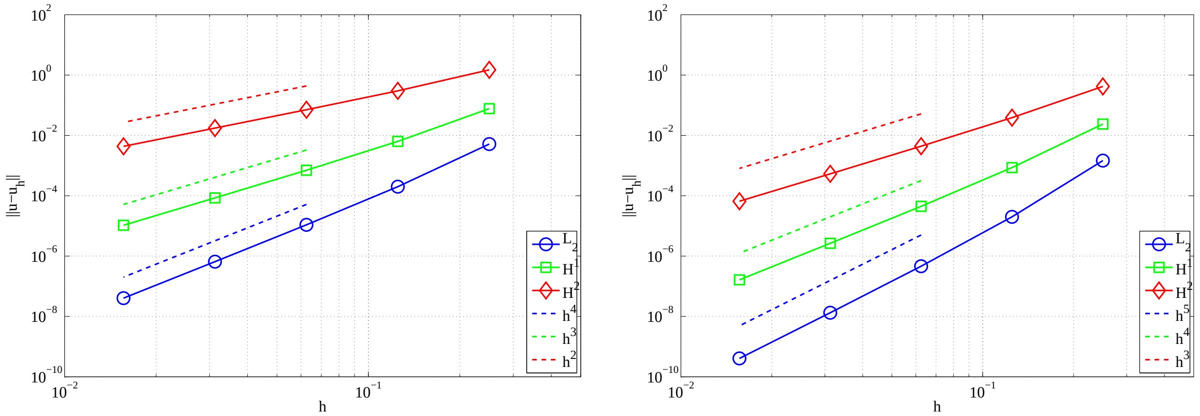

(b) $p = 3$.

(c) $p = 4$.

Figure 4: Biharmonic problem, case 1: errors in norms $L^2(\circ)$, $H^1(\square)$ and $H^2(\diamond)$ vs. the mesh size h for basis functions of degree $p = 2$ (a), $p = 3$ (b) and $p = 4$ (c); comparisons with the theoretical convergence rates.

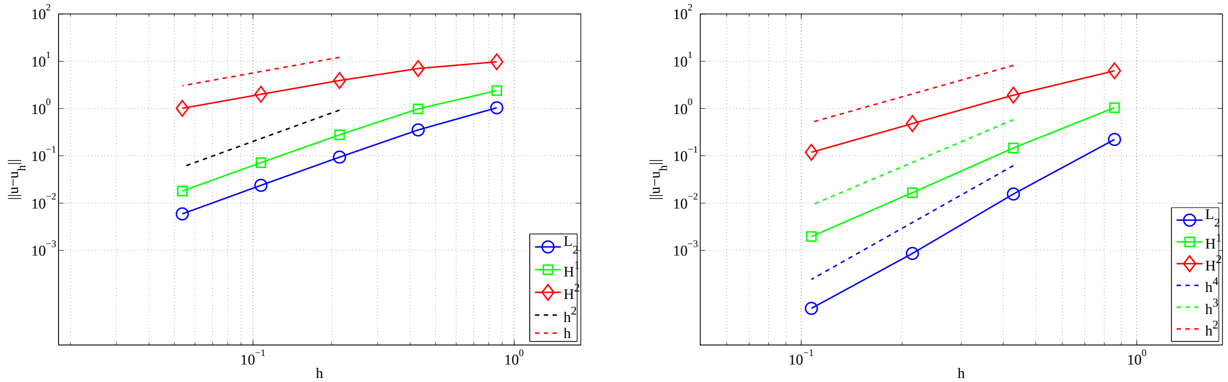

(a) $p = 2$.

(b) $p = 3$.

Figure 5: Biharmonic problem, case 2: errors in norms $L^2(\circ)$, $H^1(\square)$, and $H^2(\diamond)$ vs. the mesh size h for basis functions of degree $p = 2$ (a) and $p = 3$ (b); comparisons with the theoretical convergence rates.

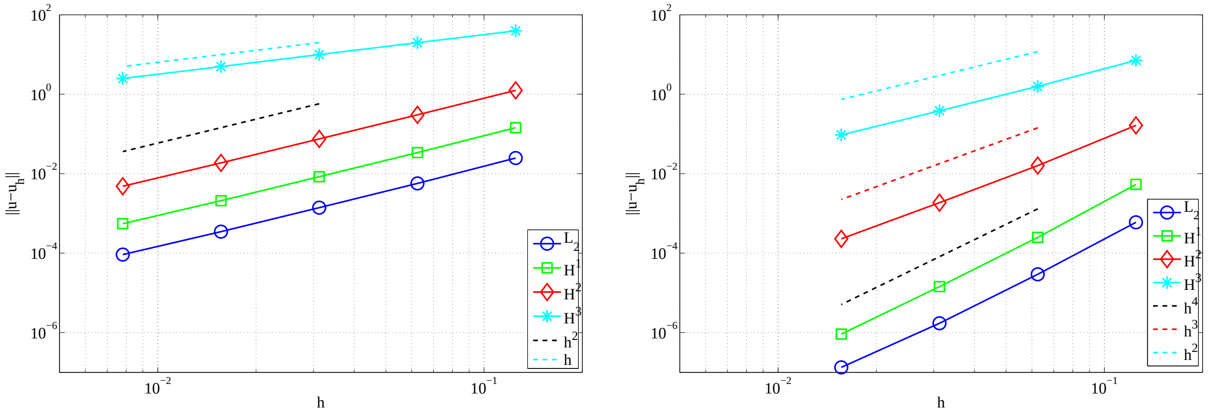

(a) $p = 3$. (b) $p = 4$.

Figure 6: Triharmonic problem: errors in norms L^2(○), H^1(□), H^2(◇), and H^3(∗) vs. the mesh size h for basis functions of degree $p = 3$ (a) and $p = 4$ (b); comparisons with the theoretical convergence rates.

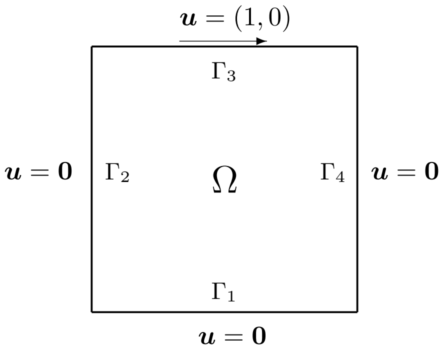

Figure 7: Lid–driven cavity problem: problem setting and data. $\Omega = (0, 1)^2$, $\Gamma_1 \cup \Gamma_2 \cup \Gamma_3 \cup \Gamma_4 = \partial\Omega$.

5.2 The lid–driven cavity problem

By considering the Navier–Stokes equations in stream function formulation (4.9), we solve the benchmark *lid–driven cavity problem* for different values of the Reynolds number ($\mathbb{R}e$). In Figure 7 we highlight the setting of the problem defined in the domain $\Omega = (0, 1)^2$ in terms of the unknown velocity field $\boldsymbol{u}$. By recalling Remark 4.1, we impose the uniqueness of the solution ψ of problem (4.9) in a classical sense, by imposing that $\psi(t) = 0$ in $(0, 0)^T$ for all $t \in (0, T)$; the (non–homogeneous) boundary conditions for the stream function thus read: $\psi|_{\partial\Omega} = 0$, $\nabla\psi \cdot \mathbf{n}|_{\Gamma_3} = 1$ and $\nabla\psi \cdot \mathbf{n}|_{\Gamma_i} = 0$ for $i = 1, 2, 4$, for all $t \in (0, T)$ [2]. We represent the computational domain $\Omega = (0, 1)^2$ by means of $\mathcal{C}^1$–continuous B–Splines basis functions of degree $p = 2$ on uniform meshes. We perform the discretization in time by means of the generalized–α method, described in Section 4.3, by setting the time step $\Delta t = 0.1$ and by choosing the parameters of the method similarly to [14, 30, 32], i.e. $\delta = \dfrac{1}{2} + \alpha_m - \alpha_f$, $\alpha_m = \dfrac{1}{2}\left(\dfrac{3 - \rho_\infty}{1 + \rho_\infty}\right)$, $\alpha_f = \dfrac{1}{1 + \rho_\infty}$, where $\rho_\infty = 0.5$. The initial condition for the stream function is $\psi(0) = \psi_0 = 0$ in Ω.

---

[2] By referring to the notation in Remark 4.1, we impose the essential boundary conditions $d_1, d_2 : \partial\Omega \times (0, T) \to \mathbb{R}$ by using a ramp function in time, i.e. we write $d_1(\mathbf{x}, t) = d_{1,S}(\mathbf{x}) d_T(t)$ and $d_2(\mathbf{x}, t) = d_{2,S}(\mathbf{x}) d_T(t)$, with $d_T(t) = \begin{cases} \dfrac{t}{0.2} & \text{if } t \leq 0.2, \\ 1 & \text{if } t > 0.2 \end{cases}$, $d_{1,S}(\mathbf{x}) = 0$ and $d_{2,S}(\mathbf{x}) = \begin{cases} 1 & \text{if } \mathbf{x} \in \Gamma_3, \\ 0 & \text{otherwise} \end{cases}$.

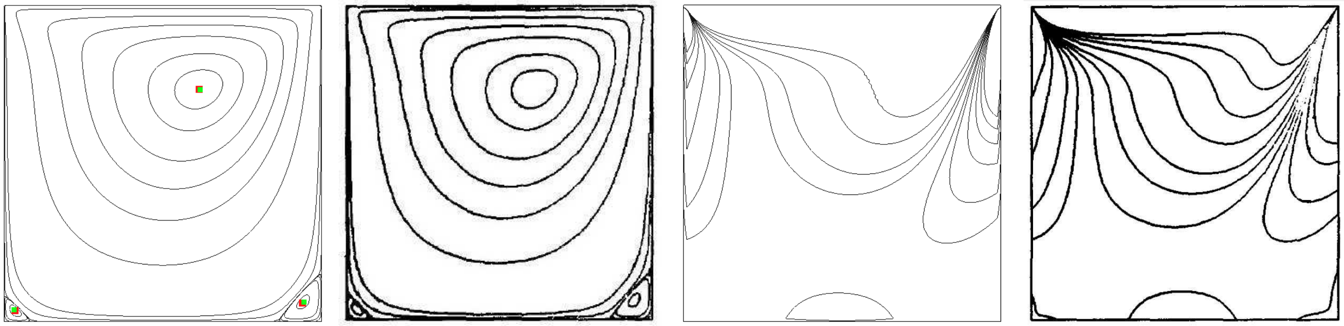

(a) Streamlines and position of vortex centers.

(b) Streamlines in [25].

(c) Vorticity contour lines.

(d) Vorticity contours in [25].

Figure 8: Lid–driven cavity problem, $\mathbb{R}e = 100$: comparison of the results at the steady state ($t = 16$) with [25]; positions of vortex centers (🟥) compared with those in [25] (🟩) (vortex centers overlap).

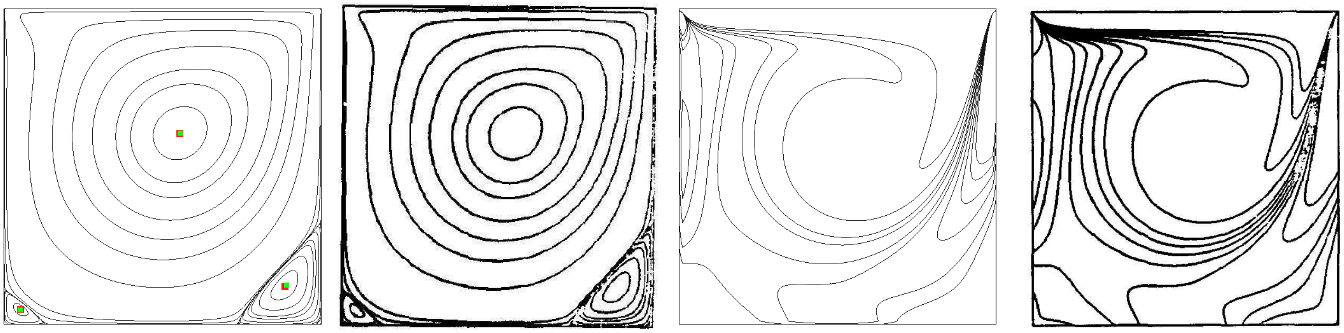

(a) Streamlines and position of vortex centers.

(b) Streamlines in [25].

(c) Vorticity contour lines.

(d) Vorticity contours in [25].

Figure 9: Lid–driven cavity problem, $\mathbb{R}e = 400$: comparison of the results at the steady state ($t = 40$) with [25]; positions of vortex centers (🟥) compared with those in [25] (🟩) (vortex centers overlap).

For each value of the Reynolds number under consideration, namely $\mathbb{R}e = 100$, 400, 1,000, and 5,000, we compare the solutions obtained at the steady state with the results in [10], [22] and [25]. We recall that the results in [25] are obtained by means of a multigrid technique ([45]) applied to finite difference schemes (specifically, a second–order accurate central finite difference scheme for second order derivatives and a first–order accurate upwind difference scheme for the convective terms); these results constitute a classical reference. In addition, similar results have been obtained in [10] by means of a spectral Chebychev collocation method. More recently, in the framework of IGA, the solution of the steady Navier–Stokes equations in primitive variables for the benchmark lid–driven cavity problem has been proposed in [22]; in this work, a divergence–conforming B–Splines discretization is used, leading to the exact pointwise satisfaction of the mass conservation property. We observe that the latter approach considers the definition of a compatible divergence–free B–Splines (NURBS) function space, whose construction is based on stream function arguments. On the other hand, we recall that when approximating the Navier–Stokes equations (4.7) in the classical weak formulation in the primitive variables $\boldsymbol{u}$ and p, suitable stabilization terms should be added in order to satisfy the discrete inf–sup condition or a compatible pair of function spaces should be introduced.

In Figures 8, 9, 10 and 11 we compare the streamlines, the vorticity contour lines, and the positions of the vortex centers with those reported in [25]. Our results are obtained with a uniform mesh of size $h = 1/256$ and a number of elements $N_{el} = 256 \times 256$, which corresponds to a total number of degrees of freedom equal to 66,564. In [25], the results for $\mathbb{R}e = 100$, 400 and 1,000 are obtained with a grid with 129×129 nodes,

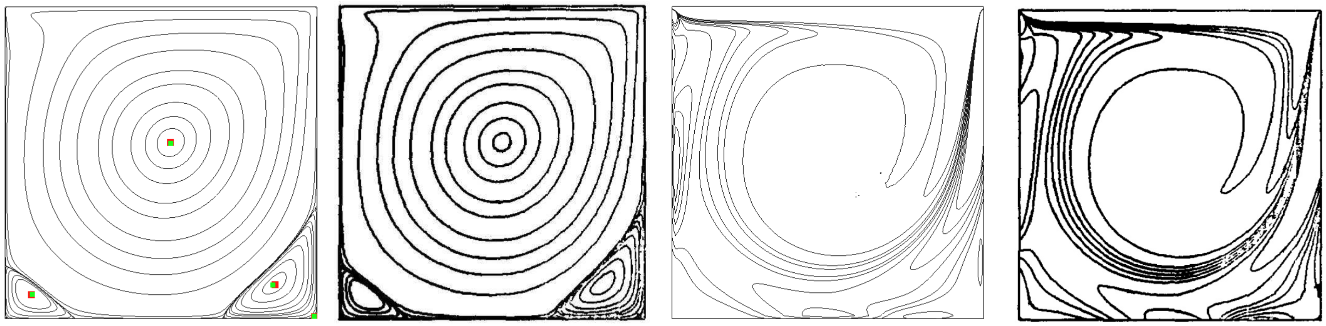

(a) Streamlines and position of vortex centers. (b) Streamlines in [25]. (c) Vorticity contour lines. (d) Vorticity contours in [25].

Figure 10: Lid–driven cavity problem, $\mathbb{R}e = 1{,}000$: comparison of the results at the steady state ($t = 40$) with [25]; positions of vortex centers (🟥) compared with those in [25] (🟩) (vortex centers overlap).

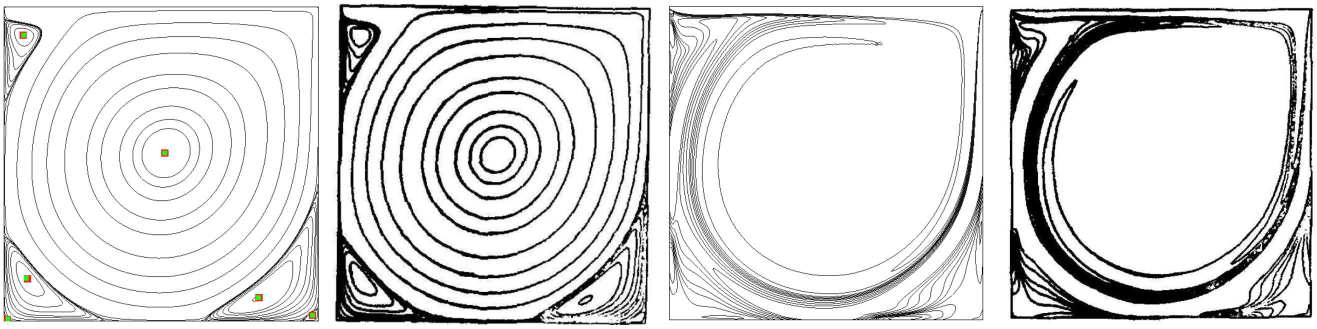

(a) Streamlines and position of vortex centers. (b) Streamlines in [25]. (c) Vorticity contour lines. (d) Vorticity contours in [25].

Figure 11: Lid–driven cavity problem, $\mathbb{R}e = 5{,}000$: comparison of the results at the steady state ($t = 192$) with [25]; positions of vortex centers (🟥) compared with those in [25] (🟩) (vortex centers overlap).

while for $\mathbb{R}e = 5{,}000$ a grid comprised of 257×257 nodes has been used in order to capture the secondary vortexes. The values of the stream function and the vorticity contour lines used for Figures 8, 9, 10 and 11 are the same highlighted in Table III of [25]. We observe that the results are qualitatively similar to those reported in [25], even for high Reynolds numbers. A qualitative difference can be observed in the vorticity contour lines obtained for $\mathbb{R}e = 5{,}000$; however a profile similar to the one shown in Figure 11c is reported in the more recent work [11], where the authors consider a finite difference discretization for the spatial approximation and a multigrid solver with a cell–by–cell relaxation procedure. Specifically, we refer to the results reported in [11] for $\mathbb{R}e = 5{,}000$ which are computed on a (much finer) grid of 2048×2048 nodes.

As reported in [11, 25], the number of regions in which the vortexes develop increases with the Reynolds number, specifically at the corners of the domain. For example, for $\mathbb{R}e = 5{,}000$, we can observe in Figure 11 that two secondary vortexes in the bottom corners and a third vortex in the upper right corner appear with respect to lower Reynolds numbers. When the Reynolds number increases, the centers of the primary and the secondary vortexes move towards the center of the domain. Moreover, the vortexes are progressively generated starting from the primary vortex. For $\mathbb{R}e = 5{,}000$, we show in Figure 12 the evolution of the streamlines from the initial condition towards the steady state. We notice that the generation of all the vortexes occurs in a relative short interval of time; then, progressively, the solution approaches to the steady state. Moreover, we observe that the two vortexes developing at the bottom right corner in Figure 12b progressively merge into a unique vortex in Figure 12c, identified as the first bottom–right vortex.

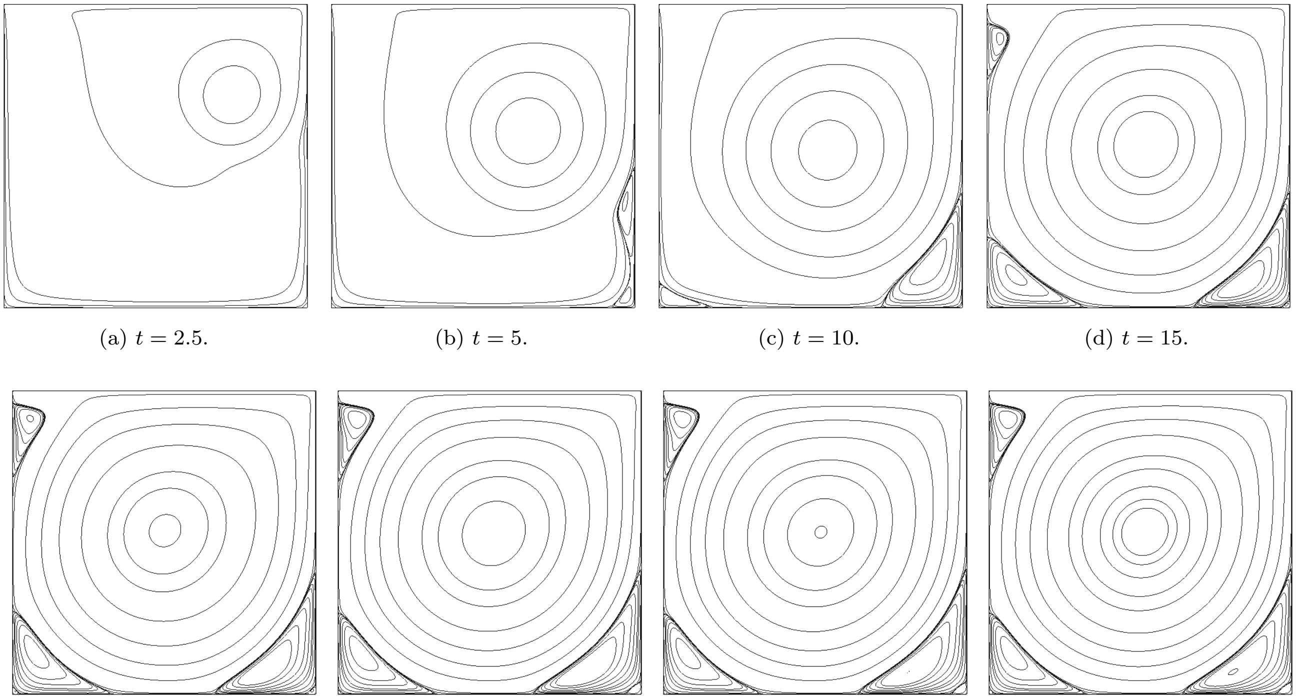

(a) $t = 2.5$. (b) $t = 5$. (c) $t = 10$. (d) $t = 15$.

(e) $t = 23$. (f) $t = 50$. (g) $t = 100$. (h) $t = 192$.

Figure 12: Lid–driven cavity problem, $\mathbb{R}e = 5{,}000$: streamlines computed at different time steps.

Table 1: Lid–driven cavity problem: vortex centers compared with [25]. Results for B–Splines basis functions of degree $p = 2$ on uniform mesh of size $h = 1/256$.

		$\mathbb{R}e = 100$		$\mathbb{R}e = 400$	
vortex	property	result	[25]	result	[25]
Primary	$\psi_{\min}$	$-1.03518 \cdot 10^{-1}$	$-1.03423 \cdot 10^{-1}$	$-1.14031 \cdot 10^{-1}$	$-1.13909 \cdot 10^{-1}$
	coordinate x	0.6150	0.6172	0.5550	0.5547
	coordinate y	0.7350	0.7344	0.6050	0.6055
First BL	$\psi_{\max}$	$1.74945 \cdot 10^{-6}$	$1.74877 \cdot 10^{-6}$	$1.40617 \cdot 10^{-5}$	$1.41951 \cdot 10^{-5}$
	coordinate x	0.0341	0.0313	0.0512	0.0508
	coordinate y	0.0346	0.0391	0.0472	0.0469
First BR	$\psi_{\max}$	$1.26045 \cdot 10^{-5}$	$1.25374 \cdot 10^{-5}$	$6.43012 \cdot 10^{-4}$	$6.42352 \cdot 10^{-4}$
	coordinate x	0.9400	0.9453	0.8850	0.8906
	coordinate y	0.0600	0.0625	0.1200	0.1250

		$\mathbb{R}e = 1{,}000$		$\mathbb{R}e = 5{,}000$	
vortex	property	result	[25]	result	[25]
Primary	$\psi_{\min}$	$-1.18511 \cdot 10^{-1}$	$-1.17929 \cdot 10^{-1}$	$-1.20245 \cdot 10^{-1}$	$-1.18966 \cdot 10^{-1}$
	coordinate x	0.5300	0.5313	0.5118	0.5117
	coordinate y	0.5650	0.5625	0.5355	0.5352
First T	$\psi_{\max}$	–	–	$1.41812 \cdot 10^{-3}$	$1.45464 \cdot 10^{-3}$
	coordinate x	–	–	0.0600	0.0625
	coordinate y	–	–	0.9100	0.9102
First BL	$\psi_{\max}$	$2.28653 \cdot 10^{-4}$	$2.31129 \cdot 10^{-4}$	$1.382460 \cdot 10^{-3}$	$1.36119 \cdot 10^{-3}$
	coordinate x	0.0834	0.0859	0.0750	0.0703
	coordinate y	0.0777	0.0781	0.1350	0.1367
First BR	$\psi_{\max}$	$1.71599 \cdot 10^{-3}$	$1.75102 \cdot 10^{-3}$	$3.05023 \cdot 10^{-3}$	$3.08358 \cdot 10^{-3}$
	coordinate x	0.8650	0.8594	0.8100	0.8086
	coordinate y	0.1100	0.1094	0.0750	0.0742
Second BL	$\psi_{\min}$	–	–	$-3.40715 \cdot 10^{-8}$	$-7.08860 \cdot 10^{-8}$
	coordinate x	–	–	0.0100	0.0117
	coordinate y	–	–	0.0050	0.0078
Second BR	$\psi_{\min}$	$-1.36433 \cdot 10^{-8}$	$-9.31929 \cdot 10^{-8}$	$-1.26084 \cdot 10^{-6}$	$-1.43226 \cdot 10^{-6}$
	coordinate x	0.9930	0.9922	0.9800	0.9805
	coordinate y	0.0070	0.0078	0.0199	0.0195

In Table 1 we compare the positions of the vortex centers and the corresponding values assumed by the stream function ψ with the results reported in [25]. We observe that there are not significant quantitative differences both for the values of the stream function and for the positions of the vortex centers. The notation is the same reported in [25]; in particular, when referring to the vortexes the letters B, L, and R denote the bottom, left, and right corners, respectively.

Table 2: Lid–driven cavity problem: velocities computed through the centerlines of the cavity compared with [10] and [25], where available. Results for B–Splines basis functions of degree $p = 2$ on uniform mesh of size $h = 1/256$.

		$\mathbb{R}e = 100$			$\mathbb{R}e = 400$	
centerline	property	result	[10]	[25]	result	[25]
Vertical	$u_{\mathrm{x}_{\min}}$	−0.21402	−0.21404	−0.21090	−0.32880	−0.32726
(x = 0.5)	coordinate y	0.4600	0.4581	0.4531	0.2800	0.2813
Horizontal	$u_{\mathrm{y}_{\min}}$	−0.25371	−0.25380	−0.24533	−0.45386	−0.44993
(y = 0.5)	coordinate x	0.8100	0.8104	0.8047	0.8600	0.8594
	$u_{\mathrm{y}_{\max}}$	0.17953	0.17957	0.17527	0.30393	0.30203
	coordinate x	0.2350	0.2370	0.2344	0.2250	0.2266

		$\mathbb{R}e = 1{,}000$			$\mathbb{R}e = 5{,}000$	
centerline	property	result	[10]	[25]	result	[25]
Vertical	$u_{\mathrm{x}_{\min}}$	−0.38754	−0.38853	−0.38289	−0.44804	−0.43643
(x = 0.5)	coordinate y	0.1700	0.1717	0.1719	0.0750	0.0703
Horizontal	$u_{\mathrm{y}_{\min}}$	−0.52582	−0.52707	−0.51550	−0.57339	−0.55408
(y = 0.5)	coordinate x	0.9100	0.9092	0.9063	0.9550	0.9531
	$u_{\mathrm{y}_{\max}}$	0.37572	0.37694	0.37095	0.44724	0.43648
	coordinate x	0.1600	0.1578	0.1563	0.0799	0.0781

In Table 2 we report a comparison between the horizontal component of the velocity field u_{x} along the vertical centerline of the domain and the vertical component of the velocity field u_{y} along the horizontal centerline of the domain with respect to data in [10] and [25], where available. Our results are obtained for uniform meshes of size $h = 1/256$. The results of [25] are computed with the same discretization already mentioned for the comparisons of Figures 8–11, whereas we consider the results presented in [10] obtained by using a pure single–domain spectral method [12] using a Gauss-Lobatto grid with 97×97 nodes, corresponding to the degree 96 for the polinomial approximation.

Moreover, in Table 3 we compare the velocities values computed for different mesh sizes in order to evaluate the sensitivity of the results with respect to the discretization, in parallel with the analysis performed in [22]. Specifically, we use B-Splines basis of degree $p = 2$ on uniform meshes of size $h = 1/(2^N)$ for $N = 6, 7, 8$, while in [22] divergence–conforming B-Splines discretizations of polynomial degree $p = 1$ on uniform meshes of size $h = 1/(2^N)$, for $N = 5, 6, 7$, are used. For the sake of completeness, we recall that we are solving the lid–driven cavity problem in terms of the stream function, whereas in [22] the problem is formulated in primitive variables $\boldsymbol{u}$ and p. We notice that, as in [22], the absolute values of both the minimum of u_{x} along the vertical centerline and the maximum and minimum of u_{y} along the horizontal centerline tend to decrease when increasing the number of degrees of freedom. The analogies highlighted in Table 3 between our results and [22] could be explained by the fact that both the approaches consider NURBS–based IGA in the framework of the Galerkin method for the spatial approximation with the exact mass conservation property satisfied by construction.

In Figure 13 we plot the components of the velocity along the respective axes for the different meshes considered, namely with mesh size $h = 1/(2^N)$, for $N = 6, 7, 8$. As underlined in [25], these plots highlight the thinning of the wall boundary layer, for increasing Reynolds numbers. As in the case of the streamlines and the vorticity contour lines, we can observe that they are in agreement with the profiles reported in literature, namely [22] and [25]. In particular, despite the presence of high gradients near the boundary, we are able to properly capture the correct behavior of the solution without resorting to stretched meshes, as in

Table 3: Lid–driven cavity problem: velocities computed through the centerlines of the cavity compared with [22] (where available) for different mesh sizes $h = 1/(2^N)$, with $N = 5, 6, 7, 8$. Results for B–Splines basis functions of degree $p = 2$, whereas in [22] compatible B–Splines basis of degree $p = 1$ are used.

	$\mathbb{R}e = 100$					
	result			[22]		
mesh size (h)	$u_{\mathrm{x}_{\min}}$	$u_{\mathrm{y}_{\min}}$	$u_{\mathrm{y}_{\max}}$	$u_{\mathrm{x}_{\min}}$	$u_{\mathrm{y}_{\min}}$	$u_{\mathrm{y}_{\max}}$
1/32	–	–	–	−0.21551	−0.25472	0.18054
1/64	−0.21442	−0.25398	0.17992	−0.21443	−0.25409	0.17991
1/128	−0.21411	−0.25380	0.17963	−0.21414	−0.25387	0.17966
1/256	−0.21402	−0.25371	0.17953	–	–	–

	$\mathbb{R}e = 400$					
	result			[22]		
mesh size (h)	$u_{\mathrm{x}_{\min}}$	$u_{\mathrm{y}_{\min}}$	$u_{\mathrm{y}_{\max}}$	$u_{\mathrm{x}_{\min}}$	$u_{\mathrm{y}_{\min}}$	$u_{\mathrm{y}_{\max}}$
1/32	–	–	–	−0.33651	−0.45768	0.31039
1/64	−0.33126	−0.45682	0.30628	−0.33150	−0.45659	0.30605
1/128	−0.32929	−0.45439	0.30442	−0.32989	−0.45470	0.30471
1/256	−0.32880	−0.45386	0.30393	–	–	–

	$\mathbb{R}e = 1{,}000$					
	result			[22]		
mesh size (h)	$u_{\mathrm{x}_{\min}}$	$u_{\mathrm{y}_{\min}}$	$u_{\mathrm{y}_{\max}}$	$u_{\mathrm{x}_{\min}}$	$u_{\mathrm{y}_{\min}}$	$u_{\mathrm{y}_{\max}}$
1/32	–	–	–	−0.40140	−0.54261	0.39132
1/64	−0.39580	−0.53468	0.38436	−0.39399	−0.53353	0.38229
1/128	−0.39027	−0.52873	0.37873	−0.39021	−0.52884	0.37856
1/256	−0.38754	−0.52582	0.37572	–	–	–

	$\mathbb{R}e = 5{,}000$					
	result			[22]		
mesh size (h)	$u_{\mathrm{x}_{\min}}$	$u_{\mathrm{y}_{\min}}$	$u_{\mathrm{y}_{\max}}$	$u_{\mathrm{x}_{\min}}$	$u_{\mathrm{y}_{\min}}$	$u_{\mathrm{y}_{\max}}$
1/64	−0.48586	−0.61218	0.48570	–	–	–
1/128	−0.45774	−0.58422	0.45796	–	–	–
1/256	−0.44804	−0.57339	0.44724	–	–	–

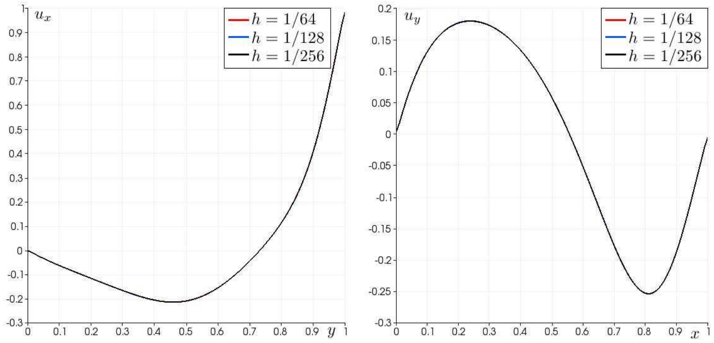

(a) $\mathbb{R}e = 100$.

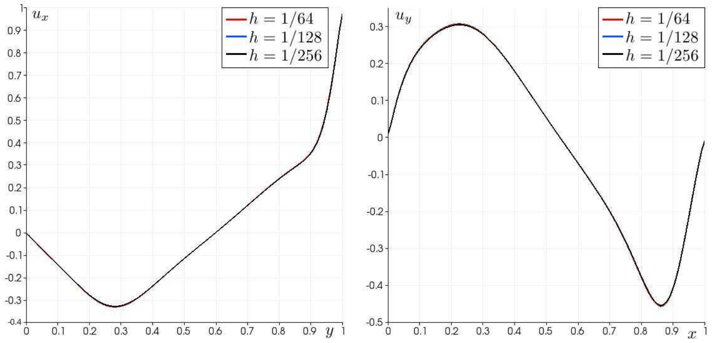

(b) $\mathbb{R}e = 400$.

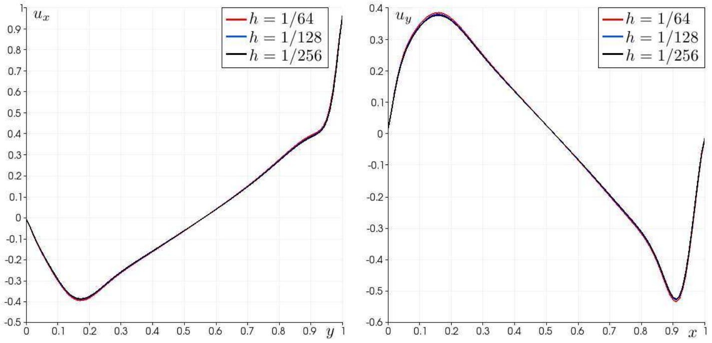

(c) $\mathbb{R}e = 1{,}000$.

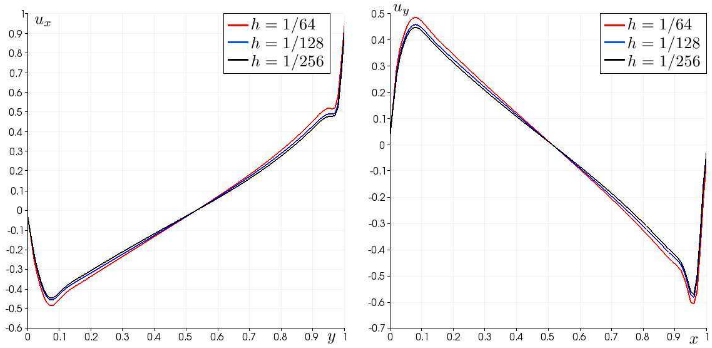

(d) $\mathbb{R}e = 5{,}000$.

Figure 13: Lid–driven cavity problem: velocities computed through the centerlines of the cavity with different mesh sizes $h = 1/(2^N)$, with $N = 6\ (-), 7\ (-), 8\ (-)$ and for B–Splines basis functions of degree $p = 2$. Horizontal component u_x of the velocity field along the vertical centerline vs. the coordinate y (left) and vertical component u_y of the velocity field along the horizontal centerline vs. the coordinate x (right), for different values of the Reynolds number $\mathbb{R}e = 100$ (a), $\mathbb{R}e = 400$ (b), $\mathbb{R}e = 1{,}000$ (c), and $\mathbb{R}e = 5{,}000$ (d).

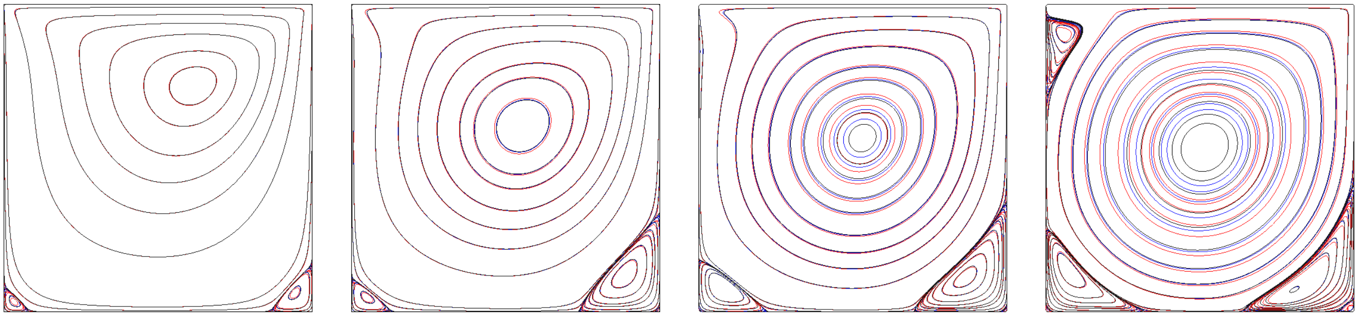

(a) $\mathbb{R}e = 100$.
(b) $\mathbb{R}e = 400$.
(c) $\mathbb{R}e = 1{,}000$.
(d) $\mathbb{R}e = 5{,}000$.

Figure 14: Lid–driven cavity problem: streamlines computed with different mesh sizes $h = 1/(2^N)$ for $N = 6$ (−), 7 (−), 8 (−) and for B–Splines basis functions of degree $p = 2$. Different values of the Reynolds number $\mathbb{R}e = 100$ (a), $\mathbb{R}e = 400$ (b), $\mathbb{R}e = 1{,}000$ (c), and $\mathbb{R}e = 5{,}000$ (d) have been considered.

e.g. [25]. We can also observe that the velocity profiles tend to exhibit a significant sensitivity with respect to the mesh size, especially for high Reynolds numbers ($\mathbb{R}e = 5{,}000$). Nevertheless, as observed in [25], the sensitivity to the mesh size h increases especially in relation with the counter-rotating vortexes near the cavity corners for high Reynolds numbers. Specifically, for the cases herein discussed, we observe that the secondary vortexes for $\mathbb{R}e = 5{,}000$ can only be captured when using fine meshes. With this aim, in Figure 14 we compare the streamlines at the steady state for different values of the mesh size, namely with mesh size $h = 1/(2^N)$, with $N = 6, 7, 8$. We observe that there are significant differences between the contour lines of the stream function in the region proximal to the primary vortex for high Reynolds numbers ($\mathbb{R}e = 1{,}000$ and $\mathbb{R}e = 5{,}000$). Moreover, we notice that for $h = 1/64$ the secondary bottom–right vortex is not captured, while it is well captured when using a mesh size $h = 1/128$. We remark that we are able to capture this feature with a coarser discretization than [25], where 66,049 degrees of freedom have been used for the case $\mathbb{R}e = 5{,}000$, conversely to our case for which the total number of degrees of freedom is equal to 15,876.

6 Conclusions

In this work, we reviewed the numerical approximation of high order PDEs by means of NURBS–based IGA in the framework of the Galerkin method. We proposed a priori error estimates for high order PDEs extending the existing results for the NURBS–based IGA–Galerkin method for the approximation of second order PDEs [3]. In particular, we focused on error estimates in lower order norms under h–refinement. We validated our error estimates by numerically solving benchmark high order elliptic PDEs, from which we obtained the expected theoretical convergence rates. As application, we considered the solution of the Navier–Stokes equations in stream function formulation, which yields a fourth order scalar problem in two dimensions. We solved the benchmark lid–driven cavity problem by means of IGA and compared the results with those available in literature, namely [10, 22] and [25], for which we highlighted the accuracy of the numerical procedure even for high Reynolds numbers, up to 5,000, and using very coarse meshes.

References

[1] R.A. Adams and J.J.F. Fournier. *Sobolev Spaces.* Academic Press, New York, 2007.

[2] F. Auricchio, L. Beirão da Veiga, F. Buffa, C. Lovadina, A. Reali, and G. Sangalli. A fully “locking–free” isogeometric approach for plane linear elasticity problems: a stream function formulation. *Computer Methods in Applied Mechanics and Engineering*, **197**:160–172, 2007.

[3] Y. Bazilevs, L. Beirão da Veiga, J.A. Cottrell, T.J.R. Hughes, and G. Sangalli. Isogeometric Analysis: approximation, stability, and error estimates for h–refined meshes. *Mathematical Models and Methods in Applied Sciences*, **16**:1031–1090, 2006.

[4] Y. Bazilevs, V.M. Calo, T.J.R. Hughes, and Y. Zhang. Isogeometric fluid–structure interaction: theory, algorithms and computations. *Computational Mechanics*, **43**:3–37, 2008.

[5] Y. Bazilevs, J.R. Gohean, T.J.R. Hughes, R.D. Moser, and Y. Zhang. Patient–specific Isogeometric fluid–structure interaction analysis of thoracic aortic blood flow due to implantation of the Jarvik 2000 left ventricular assist device. *Computer Methods in Applied Mechanics and Engineering*, **198**:3534–3550, 2009.

[6] L. Beirão da Veiga, A. Buffa, J. Rivas, and G. Sangalli. Some estimates for h–p–k–refinement in Isogeometric Analysis. *Numerische Mathematik*, **118**:271–305, 2010.

[7] D.J. Benson, Y. Bazilevs, M.C. Hsu, and T.J.R. Hughes. A large deformation, rotation–free, isogeometric shell. *Computer Methods in Applied Mechanics and Engineering*, **200**:1367–1378, 2011.

[8] D.J. Benson, Y. Bazilevs, M.C. Hsu, and T.J.R. Hughes. Isogeometric shell analysis: the Reissner–Mindlin shell. *Computer Methods in Applied Mechanics and Engineering*, **199**:276–289, 2010.

[9] M.J. Borden, C.V. Verhoosel, M.A. Scott, T.J.R. Hughes, and C.M. Landis. A phase–field description of dynamic brittle fracture. *Computer Methods in Applied Mechanics and Engineering*, **217–220**:77–95, 2012.

[10] O. Botella and R. Peyret. Benchmark spectral results on the lid–driven cavity flow. *Computers & Fluids*, **27**:421–433, 1998.

[11] C.H. Bruneau and M. Saad. The 2D lid–driven cavity problem revisited. *Computers & Fluids*, **35**:326–348, 2006.

[12] C. Canuto, M.Y. Hussaini, A. Quarteroni, and T.A. Zang. *Spectral Methods. Fundamentals in Single Domains.* Springer–Verlag, Berlin and Heidelberg, 2006.

[13] Z. Chen. *Finite Element Methods and their Applications.* Springer–Verlag, Berlin, 2005.

[14] J. Chung and G.M. Hulbert. A time integration algorithm for structural dynamics with improved numerical dissipation: the generalized–α method. *Journal of Applied Mechanics*, **60**:371–375, 1993.

[15] B. Cockburn and C.W. Shu. The local discontinuous Galerkin method for time–dependent convection–diffusion systems. *SIAM Journal of Numerical Analysis*, **35**, no.6, 1998.

[16] J.A. Cottrell, T.J.R. Hughes, and Y. Bazilevs. Isogeometric Analysis: CAD, finite elements, NURBS, exact geometry and mesh refinement. *Computer Methods in Applied Mechanics and Engineering*, **194**:4135–4195, 2005.

[17] J.A. Cottrell, T.J.R. Hughes, and Y. Bazilevs. *Isogeometric Analysis: Toward Integration of CAD and FEA.* John Wiley & Sons, Chichester, UK, 2009.

[18] J.A. Cottrell, T.J.R. Hughes, and A. Reali. Studies of refinement and continuity in isogeometric structural analysis. *Computer Methods in Applied Mechanics and Engineering*, **196**:4160–4183, 2007.

[19] L. Dedè, M.J. Borden, and T.J.R. Hughes. Isogeometric Analysis for topology optimization with a phase field model. *Archives of Computational Methods in Engineering*, **19**:427–465, 2012.

[20] L. Dedè and A. Quarteroni. Isogeometric Analysis for second order partial differential equations on surfaces. *MATHICSE Technical Report*, **36**, 2012.

[21] G. Engel, K. Garikipati, T.J.R. Hughes, M.G. Larson, L. Mazzei, and R.L. Taylor. Continuous/discontinuous finite element approximations of fourth–order elliptic problems in structural and continuum mechanics with applications to thin beams and plates, and strain gradient elasticity. *Computer Methods in Applied Mechanics and Engineering*, **191**:4333–4352, 2002.

[22] J.A. Evans and T.J.R. Hughes. Isogeometric divergence–conforming B–splines for the steady Navier–Stokes equations. *Mathematical Models and Methods in Applied Sciences*, **23**:1421–1478, 2013.

[23] J.A. Evans and T.J.R. Hughes. Isogeometric divergence–conforming B–Splines for the unsteady Navier–Stokes equations. *Journal of Computational Physics*, **241**:141–167, 2013.

[24] M. Fortin and F. Brezzi. *Mixed and Hybrid Finite Element Methods.* Springer, New York, 1979.

[25] U. Ghia, K.N. Ghia, and C.T. Shin. High–Re solutions for incompressible flow using the Navier–Stokes equations and a multigrid method. *Journal of Computational Physics*, **48**:387–411, 1982.

[26] V. Girault and P.A. Raviart. *Finite Element Approximation of the Navier–Stokes Equations.* Springer–Verlag, Berlin and New York, 1979.

[27] H. Gómez, V.M. Calo, Y. Bazilevs, and T.J.R. Hughes. Isogeometric Analysis of the Cahn–Hilliard phase–field model. *Computer Methods in Applied Mechanics and Engineering*, **197**:4333–4352, 2008.

[28] H. Gómez and X. Nogueira. An unconditionally energy–stable method for the phase field crystal equation. *Computer Methods in Applied Mechanics and Engineering*, **249–252**:52–61, 2012.

[29] T.J.R. Hughes. *The Finite Element Method: Linear Static and Dynamic Finite Element Analysis.* Dover Publications, Mineola, New York, 2000.

[30] K.E. Jansen, C.H. Whiting, and G.M. Hulbert. A generalized–α method for integrating the filtered Navier–Stokes equations with a stabilized finite element method. *Computer Methods in Applied Mechanics and Engineering*, **190**:305–319, 2000.

[31] J.L. Lions and E. Magenes. *Problèmes aux Limites non Homogènes et Applications.* Dunod, Paris, 1968.

[32] J. Liu, L. Dedè, J.A. Evans, M.J. Borden, and T.J.R. Hughes. Isogeometric Analysis of the advective Cahn–Hilliard equation: spinodal decomposition under shear flow. *Journal of Computational Physics*, **242**:321–350, 2013.

[33] D. Liu and G. Xu. A general sixth order geometric partial differential equation and its application in surface modeling. *Journal of Information and Computational Science*, **4**:1–12, 2007.

[34] X. Meng, C.W. Shu, and B. Wu. Superconvergence of the local discontinuous Galerkin method for linear fourth–order time–dependent problems in one space dimension. *IMA Journal of Numerical Analysis*, **32**:1294–1328, 2012.

[35] J.T. Oden. Advanced theory of finite elements: an introduction to the mathematical foundation of the Finite Element Method. *ICES Report*, Institute for Computational Engineering and Sciences, The University of Texas at Austin, **00–12**, 2000.

[36] T.N. Phillips. Pseudospectral domain decomposition techniques for the Navier–Stokes equations. In D.E. Keyes, T.F. Chan, G. Meurant, J.S. Scroggs, and R.G. Voigt. *Fifth International Symposium on Domain Decomposition Methods for Partial Differential Equations*, 531–540. SIAM Proceedings in Applied Mathematics, 1992.

[37] L. Piegl and W. Tiller. *The NURBS Book.* Springer–Verlag, New York, 1997.

[38] W. Rudin. *Principles of Mathematical Analysis.* McGraw–Hill, New York, 1976.

[39] L. Quartapelle. *Numerical Solution of the Incompressible Navier–Stokes Equations*. Birkhäuser–Verlag, Basel, 1993.

[40] A. Quarteroni. *Numerical Models for Differential Problems*. Springer–Verlag, Milan, 2009.

[41] A. Quarteroni and A. Valli. *Numerical Approximation of Partial Differential Equations*. Springer–Verlag, Berlin and Heidelberg, 1994.

[42] L.L. Schumaker. *Spline Functions: Basic Theory*. Cambridge University Press, New York, 2007.

[43] G. Strang and G. Fix. *An Analysis of the Finite Element Method*. Wellesley–Cambridge Press, Englewood Cliffs, N.J., 1973.

[44] A. Tagliabue. Isogeometric Analysis for reduced fluid–structure interaction models in haemodynamic applications. Master Degree Thesis, Università degli Studi dell'Insubria, Italy, 2012. `http://infoscience.epfl.ch/record/183031/files/thesis_tagliabue_2012.pdf`.

[45] P.S. Vassilevski. Lecture notes on Multigrid methods. *Lawrence Livermore National Laboratory*, Technical Report LLNL-TR-439511. `http://people.llnl.gov/vassilevski1`.

[46] C.V. Verhoosel, M.A. Scott, T.J.R. Hughes, and R. de Borst. An unconditionally energy–stable method for the phase field crystal equation. *International Journal for Numerical Methods in Engineering*, **86**:115–134, 2011.

[47] Y. Zhang, Y. Bazilevs, S. Goswam, C.L. Bajaj, and T.J.R. Hughes. Patient–specific vascular NURBS modeling for Isogeometric Analysis of blood flow. *Computer Methods in Applied Mechanics and Engineering*, **196**:2943–2959, 2007.

MOX Technical Reports, last issues

Dipartimento di Matematica “F. Brioschi”,
Politecnico di Milano, Via Bonardi 9 - 20133 Milano (Italy)

27/2013 Tagliabue, A.; Dedè, L.; Quarteroni, A.
Isogeometric Analysis and Error Estimates for High Order Partial Differential Equations in Fluid Dynamics

26/2013 Ieva, F.; Paganoni, A.M.
Detecting and visualizing outliers in provider profiling via funnel plots and mixed effect models

25/2013 Cattaneo, Laura; Zunino, Paolo
Computational models for coupling tissue perfusion and microcirculation

24/2013 Mazzieri, I.; Stupazzini, M.; Guidotti, R.; Smerzini, C.
SPEED-SPectral Elements in Elastodynamics with Discontinuous Galerkin: a non-conforming approach for 3D multi-scale problems

23/2013 Srensen, H.; Goldsmith, J.; Sangalli, L.M.
An introduction with medical applications to functional data analysis

22/2013 Falcone, M.; Verani, M.
Recent Results in Shape Optimization and Optimal Control for PDEs

21/2013 Perotto, S.; Veneziani, A.
Coupled model and grid adaptivity in hierarchical reduction of elliptic problems

20/2013 Azzimonti, L.; Nobile, F.; Sangalli, L.M.; Secchi, P.
Mixed Finite Elements for spatial regression with PDE penalization

19/2013 Azzimonti, L.; Sangalli, L.M.; Secchi, P.; Domanin, M.; Nobile, F.
Blood flow velocity field estimation via spatial regression with PDE penalization

18/2013 Discacciati, M.; Gervasio, P.; Quarteroni, A.
Interface Control Domain Decomposition (ICDD) Methods for Coupled Diffusion and Advection-Diffusion Problems